

# Beyond the Classical Ceiling: Multi-Layer Fully-Connected Variational Quantum Circuits

Howard Su<sup>1</sup> Chen-Yu Liu<sup>2</sup> Samuel Yen-Chi Chen<sup>3</sup> Kuan-Cheng Chen<sup>4</sup> Huan-Hsin Tseng<sup>3</sup>

## Abstract

Standard Variational Quantum Circuits (VQCs) struggle to scale to high-dimensional data due to the “curse of dimensionality,” which manifests as exponential simulation costs ( $\mathcal{O}(2^d)$ ) and untrainable Barren Plateaus. Existing solutions often bypass this by relying on classical neural networks for feature compression, obscuring the true quantum capability. In this work, we propose the **Multi-Layer Fully-Connected VQC (FC-VQC)**, a modular architecture that performs **end-to-end quantum learning** without trainable classical encoders. By restricting local Hilbert space dimensions while enabling global feature interaction via structured block mixing, our framework achieves **linear scalability**  $\mathcal{O}(d)$ . We empirically validate this approach on standard benchmarks and a high-dimensional industrial task: **300-asset Option Portfolio Pricing**. In this regime, the FC-VQC breaks the “Classical Ceiling,” outperforming state-of-the-art Gradient Boosting baselines (XGBoost/CatBoost) while exhibiting  $\approx 17\times$  **greater parameter efficiency** than Deep Neural Networks. These results provide concrete evidence that pure, modular quantum architectures can effectively learn industrial-scale feature spaces that are intractable for monolithic ansatzes.

## 1. Introduction

The pursuit of **Quantum Machine Learning (QML)** is driven by the premise that high-dimensional quantum Hilbert spaces offer representational capacities exceeding those of classical systems (Biamonte et al., 2017). **Varia-**

<sup>1</sup>Department of Computing, Imperial College London, UK

<sup>2</sup>Graduate Institute of Applied Physics, National Taiwan University, Taiwan

<sup>3</sup>Brookhaven National Laboratory, Upton, NY, USA

<sup>4</sup>Centre for Quantum Engineering, Science and Technology, Imperial College London, UK. Correspondence to: Howard Su <h.su24@imperial.ac.uk>.

**tional Quantum Circuits (VQCs)**<sup>1</sup> are the primary vehicle for this ambition (Schuld et al., 2020; Mitarai et al., 2018; Cerezo et al., 2021a; Bharti et al., 2022); theoretical analyses suggest they exhibit significantly higher effective dimension and generalization capacity than comparable classical networks (Abbas et al., 2021).

Despite these guarantees, practical implementations face a pervasive limitation we term the “**Classical Ceiling**”: a performance boundary where pure VQC architectures fail to outperform classical baselines. Recent proofs reveal this is a fundamental paradox in standard designs. Increasing circuit complexity to gain advantage leads to untrainable *barren plateaus* (McClean et al., 2018; Cerezo et al., 2021b). Conversely, simplifying the architecture to ensure trainability often collapses the model into a regime that is mathematically redundant to classical methods (Schreiber et al., 2023; Landman et al., 2023). Thus, standard VQCs are trapped: they are either too complex to train or too simple to offer any advantage, effectively locking them beneath a performance ceiling established by classical machine learning. Consequently, many studies resort to hybrid approaches that use classical neural networks (e.g., CNNs) (Mari et al., 2020) to compress input data, shifting the learning burden away from the quantum circuit.

To address this, we introduce **Multi-layer Fully-Connected Variational Quantum Circuits (FC-VQCs)**, a modular framework designed to scale beyond this ceiling without classical assistance. Our contributions are:

**End-to-End Quantum Training:** We propose a general-purpose framework built from composable  $q$ -qubit blocks. Unlike hybrid transfer learning methods, our model contains **no trainable classical encoders**. All parameters reside within the quantum circuit, ensuring that the observed performance gains stem solely from quantum expressivity.

**Linear Scalability ( $\mathcal{O}(d)$ ):** Unlike monolithic ansatzes with exponential resource scaling ( $\mathcal{O}(2^d)$ ), our modular design exhibits linear complexity. This allows effective scaling to **300 input dimensions**, maintaining stable gradients on tasks where standard VQCs fail.

<sup>1</sup>Interchangeably referred to as Parameterized Quantum Circuits (PQCs) or Quantum Neural Networks (QNNs).

**Breaking the Classical Ceiling:** We demonstrate that FC-VQCs consistently surpass Deep Neural Networks and match state-of-the-art gradient boosting ensembles (XG-Boost, CatBoost) on high-dimensional benchmarks. Notably, this parity is achieved with  $\approx 15 \times$  **greater parameter efficiency** than classical networks, validating the superior information density of the proposed quantum neurons.

## 2. Scalable Variational Quantum Architectures

The application of VQCs to high-dimensional data faces a fundamental scalability dilemma. Encoding  $\mathbf{x} \in \mathbb{R}^d$  without information loss typically requires the qubit count  $N$  to scale with  $d$ , yet optimizing monolithic global unitaries over large registers often suffers from barren plateaus, with gradients vanishing exponentially in system size (McClean et al., 2018). Practical deployment further disfavors such circuits due to limited access to large, high-fidelity processors and the depth overhead induced by noise and restricted connectivity (e.g., SWAP routing), which amplifies error accumulation on NISQ devices. As a result, many VQC studies either remain in low-dimensional regimes or rely on aggressive dimensionality reduction via PCA, classical neural encoders (Mari et al., 2020; Qi et al., 2024), or tensor-network-based mappings (Chen et al., 2021; Qi et al., 2023), potentially discarding task-relevant information; large monolithic circuits are also difficult to validate systematically because classical simulation quickly becomes prohibitive.

A natural remedy is a *modular* architecture that composes small trainable units across multiple subsystems, aligning with emerging multi-chip/multi-QPU paradigms and enabling more tractable simulation and benchmarking. Distributed approaches along this direction include federated QML (Chen & Yoo, 2021; Chehimi & Saad, 2022; Mathur et al., 2025; Chehimi et al., 2023) with server-side aggregation, often combined with CNN-based feature compression prior to a small VQC (Chen & Yoo, 2021), and multi-chip/multi-QPU designs that partition features across many shallow VQCs and aggregate measurements, effectively treating each chip as a local expert (Park et al., 2025; Chen et al., 2025). However, two gaps remain: CNN-based compression can shift substantial representation learning to the classical front-end, obscuring the quantum model’s scaling behavior, while ensemble-style multi-chip constructions without explicit inter-module mixing offer limited *layer-wise* global feature interaction. Motivated by these gaps, this work introduces a *multi-layer, fully-connected* modular VQC that preserves local trainability while systematically increasing global expressivity through structured inter-block mixing.

### 2.1. Type 1: Monolithic Single VQC

Type 1 represents the standard baseline found in most current QML literature. The model consists of a single variational quantum circuit that processes all  $d$  input features jointly in one monolithic layer ( $L = 1$ ). Concretely, we set  $q = d$  and apply a single global unitary evolution followed by measurements. Since Type 1 relies entirely on the expressivity of this single evolution, we formalize here the fundamental  $q$ -qubit VQC block (“quantum neuron”) that serves as the building block for all subsequent architectures.

#### 2.1.1. FEATURE ENCODING

Given an input vector  $h = (h_1, \dots, h_q) \in \mathbb{R}^q$ , the first step is to encode these features into a  $q$ -qubit quantum register. We employ rotation-based embedding, in which each component  $h_j$  modulates a single-qubit rotation:

$$|\psi_{enc}(h)\rangle = \bigotimes_{j=1}^q R_\alpha(h_j)|0\rangle, \quad (1)$$

where  $R_\alpha(\cdot)$  is a chosen rotation gate (e.g.,  $R_Y$ ). This produces a separable initial state whose amplitudes depend smoothly on the input features.

#### 2.1.2. VARIATIONAL STRONGLY ENTANGLING LAYERS

After encoding, the state is processed by  $K$  trainable variational layers. We employ the *StronglyEntanglingLayers* architecture proposed by (Schuld et al., 2020).

**Local parameterized rotations:** Every qubit  $j$  acts as a universal single-qubit classifier via a general rotation  $U(\theta_j^{(k)})$ , decomposed into Euler angles:

$$U(\theta_j^{(k)}) = R_Z(\omega_j^{(k)})R_Y(\theta_j^{(k)})R_Z(\phi_j^{(k)}) \quad (2)$$

Critically, this gate utilizes **three trainable parameters** per qubit  $(\omega, \theta, \phi)$ , whereas standard heuristic ansatzes typically use only one (e.g.,  $R_y(\theta)$ ). This triple parameterization allows the layer to access the full complex amplitude space of the qubit, significantly increasing the expressive power of the ansatz compared to real-valued heuristics.

**Strong Entanglement:** Non-local correlations are introduced via CNOT gates arranged in a periodic, cyclic topology determined by a layer-specific *range* parameter  $r_k$ . For every qubit  $j$ , a CNOT is applied between the control wire  $j$  and the target wire  $(j + r_k) \pmod q$ . By cycling the range  $r_k$  across layers, this topology distributes entanglement globally, wrapping around the qubit boundary to ensure no qubit is topologically isolated.

#### 2.1.3. MEASUREMENT AND CLASSICAL OUTPUT

The VQC block produces classical outputs by measuring a fixed set of observables. For  $n_{out}$  output channels, we

evaluate:

$$f_{\Theta}(h)_j = \langle \psi_{enc}(h) | U^\dagger(\Theta) O_j U(\Theta) | \psi_{enc}(h) \rangle \quad (3)$$

where each  $\langle O_j \rangle$  denotes the expectation value of a Pauli-Z observable measured on the final state.

## 2.2. Type 2: Multi-Layer Single VQC

Type 2 extends the Type 1 architecture by increasing the variational depth while maintaining a single global processing unit per layer. Instead of a single continuous variational transformation, we construct a deep model by stacking  $L \geq 2$  copies of the  $q$ -qubit VQC block (with  $q = d$ ) in series. Crucially, this architecture employs a **measure-and-re-encode** strategy to mitigate coherent noise accumulation: between layers, the quantum state is measured to extract a classical feature vector, which is then re-encoded into the subsequent block. Let  $H^{(0)} = x \in \mathbb{R}^d$  be the input feature vector. The forward pass is defined recursively for layers  $l = 1, \dots, L$ :

$$H^{(l)} = f_{\Theta^{(l)}}(H^{(l-1)}), \quad (4)$$

where  $f_{\Theta^{(l)}} : \mathbb{R}^d \rightarrow \mathbb{R}^d$  denotes the global  $q$ -qubit quantum neuron defined in Section 2.1, parameterized by a distinct set  $\Theta^{(l)}$  at each layer. The final model output is the result of this sequential composition:

$$H^{(L)} = f_{\Theta^{(L)}}(\dots f_{\Theta^{(2)}}(f_{\Theta^{(1)}}(x)) \dots). \quad (5)$$

Type 2 aims to increase representational power solely through the depth of stacked global quantum transformations, without introducing any architectural structure beyond a single monolithic block.

## 2.3. Type 3: Multi-Layer Fully-Connected VQCs

Type 3 is our proposed architecture. It generalizes the classical multilayer perceptron by replacing classical neurons with the  $q$ -qubit quantum neurons defined in Section 2.1, arranged in a structured multi-block topology. Crucially, all trainable parameters reside within the quantum circuits; inter-block connectivity is realized by deterministic, parameter-free block-mixing rules. This yields a fully quantum deep architecture rather than a hybrid quantum-classical network.

### 2.3.1. INPUT LAYER

Let the model input be a feature vector  $x \in \mathbb{R}^d$ . We assume  $d = Bq$ , where  $q$  is the number of qubits per VQC block and  $B$  is the number of blocks in the layer. The input layer partitions the vector into  $B$  contiguous blocks of width  $q$ :

$$x = [x^{(1)}, x^{(2)}, \dots, x^{(B)}], \quad x^{(b)} \in \mathbb{R}^q. \quad (6)$$

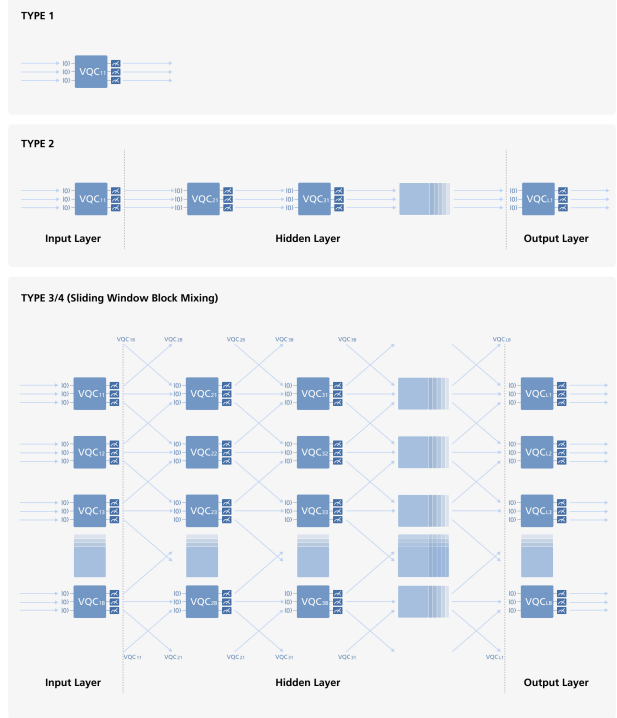


Figure 1. Overview of Scalable VQC Architectures.

Each block  $x^{(b)}$  is independently processed by a  $q$ -qubit variational quantum circuit using the map  $f_{\Theta}$  defined in Section 2.1. Thus, the input layer performs:

$$h^{(1,b)} = f_{\Theta_b^{(0)}}(x^{(b)}), \quad b = 1, \dots, B, \quad (7)$$

where  $\Theta_b^{(0)}$  denotes the trainable parameters associated with block  $b$  in the input layer. The output of the input layer is obtained by concatenating the  $B$  quantum outputs, preserving the global feature dimension.

### 2.3.2. HIDDEN LAYERS AND BLOCK MIXING

Let the input to the  $l$ -th hidden layer be the block-structured vector  $H^{(l)} = [h^{(l,1)}, \dots, h^{(l,B)}]$ . Before processing the next layer, the model constructs a new set of block inputs  $\tilde{h}^{(l,b)}$  using a deterministic *block-mixing rule*:

$$\tilde{h}^{(l,b)} = g_b^{(l)}(h^{(l,1)}, \dots, h^{(l,B)}) \quad (8)$$

which redistributes information across blocks. This reshaping plays the role of the weight matrix in a classical fully connected layer, enabling global feature interaction while keeping the quantum units fixed at size  $q$ . We utilize three primary mixing rules:

**Fully Connected Block Mixing:** Conceptually, the most expressive choice allows each block in layer  $l+1$  to receive information from all blocks in layer  $l$ . A simple realization

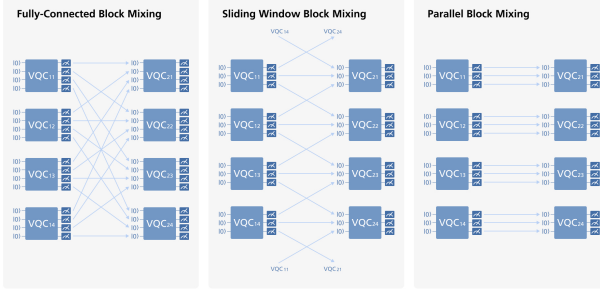


Figure 2. Block Mixing Rules.

arises when  $d = q^2$  (so  $B = q$ ), allowing each next-layer input to draw one component from every block:

$$\tilde{h}^{(l,b)} = [h_j^{(l,1)}, h_j^{(l,2)}, \dots, h_j^{(l,q)}] \quad (9)$$

This produces fully connected interactions between blocks, serving as the quantum analogue of a dense classical layer.

**Sliding-Window Block Mixing:** To accommodate high-dimensional inputs while retaining effective information flow, we adopt a structured local mixing pattern. First, it is preferred that the number of qubits  $q$  in the VQC block be an **odd number**. This allows for symmetric sliding windows, where the central target block collects components from an equal number of left and right neighbors. For an odd  $q$ , the next-layer input at block  $b$  is formed by collecting components from  $(q-1)/2$  neighboring blocks:

$$\tilde{h}^{(l,b)} = [h^{(l,b-(q-1)/2)}, \dots, h^{(l,b)}, \dots, h^{(l,b+(q-1)/2)}]. \quad (10)$$

Second, to handle the edges of the block array (e.g.,  $b_{start}$  and  $b_{end}$ ), we implement a **ring topology** (circular mixing). The boundaries are connected such that the first block  $b_{start}$  draws input components from the last block  $b_{end}$ , and conversely,  $b_{end}$  draws from  $b_{start}$ . This ensures that no block is topologically isolated and that information propagates globally across the ring over multiple layers.

**Parallel Block Mixing:** This strategy enforces strict independence between blocks, functioning as an ensemble of disjoint quantum circuits. We set the mixing operation to the identity:

$$\tilde{h}^{(l,b)} = h^{(l,b)}. \quad (11)$$

No information is exchanged between parallel blocks. This structure is particularly effective for problems where the input features are statistically independent, as it prevents the “over-entanglement” of uncorrelated data streams while allowing deep processing within each independent channel.

Once the mixed blocks are constructed, each is processed by its own VQC block,  $h^{(l+1,b)} = f_{\Theta_b^{(l)}}(\tilde{h}^{(l,b)})$ , and the results are concatenated to form the layer output.



Figure 3. Schematic plot of 9t3t1

### 2.3.3. OUTPUT LAYER

The output layer transforms the final hidden representation into the model prediction. As in the preceding layers, this transformation is implemented entirely by VQCs; no classical affine mappings and activation functions are introduced. Let  $H^{(L)}$  denote the output of the last hidden layer. Depending on the desired output dimension, we consider two cases:

**Dimension-Preserving Output:** If the prediction dimension matches the input or hidden-layer dimension (typically  $d = Bq$ ), each block acts independently to produce  $n_{out} = q$  expectation values. The final layer output is the concatenation of these block outputs:

$$H^{(L)} = [f_{\Theta_1^{(L)}}(h^{(L,1)}), \dots, f_{\Theta_B^{(L)}}(h^{(L,B)})] \in \mathbb{R}^d. \quad (12)$$

This configuration is particularly useful for time series models (e.g., forecasting state vectors at each time step) or high-dimensional differential equation solvers (Su & Tseng, 2025) where the output dimension is the same or similar to the input dimension.

**Multi-Stage Dimensionality Reduction:** For high-dimensional inputs requiring a lower-dimensional output (e.g., regression or classification), we stack layers to progressively compress features ( $\mathbb{R}^d \rightarrow \dots \rightarrow \mathbb{R}^{d_{out}}$ ). This is achieved by measuring fewer observables than the number of encoded qubits ( $n_{out} < q$ ).

We denote this topology as  $d_{in}td_1t\dots td_{out}$ , where ‘ $t$ ’ represents the transition between layers. For example, a **27t9t3t1** architecture reduces  $d = 27$  features in three stages ( $27 \rightarrow 9 \rightarrow 3 \rightarrow 1$ ). In the first stage,  $q = 3$  qubits encode the data, but only  $n_{out} = 1$  value is measured per block, effectively performing a quantum pooling operation that reduces the dimension by a factor of 3 at each layer. Schematic plot of the **9t3t1** architecture (see Fig. 3).

## 2.4. Type 4: Extended Multi-Layer Fully-Connected VQCs

Standard block-based architectures are limited on low-dimensional datasets ( $d < 10$ ) due to restricted network width ( $B = d/q$ ). To decouple model complexity from input dimensionality, Type 4 expands the feature space to

$d_{ext} = m \cdot d$  via an extended feature map  $\tilde{x} = \phi_{ext}(x) \in \mathbb{R}^{d_{ext}}$ . We construct  $\tilde{x}$  by concatenating deterministic non-linear transformations—such as high-order polynomials  $(x, x^2, \dots)$ , low-order roots  $(x, x^{0.5}, \dots)$ , or logarithms  $(x, \log x, \dots)$ —thereby strictly increasing the number of trainable VQC blocks and expressive power.

#### 2.4.1. BLOCK PARTITIONING AND QUANTUM PROCESSING

The extended vector  $\tilde{x}$  is processed into a standard Type 3 FC-VQC architecture. We choose a block width  $q$  such that  $d_{ext} = q \times B_{ext}$  and partition  $\tilde{x}$  into  $B_{ext}$  contiguous blocks:

$$\tilde{x} = [\tilde{x}^{(1)}, \tilde{x}^{(2)}, \dots, \tilde{x}^{(B_{ext})}], \quad \tilde{x}^{(b)} \in \mathbb{R}^q. \quad (13)$$

These blocks are processed exactly the same as Type 3.

#### 2.4.2. BLOCK PARTITIONING AND EXPRESSIVE CAPACITY

The extended vector  $x$  is partitioned into  $B_{ext} = d_{ext}/q$  blocks and processed via the Type 3 architecture. The critical advantage of this expansion is the decoupling of model depth from input dimensionality: since  $d_{ext} > d$ , the network contains significantly more VQC blocks ( $B_{ext} > B$ ). Because the total parameter count scales linearly with the number of blocks, this mechanism allows us to arbitrarily increase the parameter budget. Even though the underlying data lies in a low-dimensional manifold, VQC blocks operating on transformed features (e.g.,  $x^{0.5}$  or  $\log x$ ) can capture complex correlations inaccessible to a single narrow quantum neuron.

### 2.5. Computational Complexity on Classical Simulators

While designed for quantum hardware, the modular structure of the FC-VQC framework yields a distinct advantage for classical simulation. Standard monolithic VQCs (Type 1 & 2) process  $d$  features in a single register, requiring state vectors of size  $2^d$ . This results in an exponential simulation complexity of  $\mathcal{O}_{\text{mono}} \propto L \cdot 2^d$ , creating a hard ceiling for high-dimensional tasks.

In contrast, the FC-VQC (Type 3 & 4) partitions the circuit into  $B = d/q$  independent blocks of fixed size  $q$ . Due to the measure-and-re-encode strategy, a simulator need only maintain state vectors of size  $2^q$ . The total complexity becomes the sum over blocks:  $\mathcal{O}_{\text{mod}} = L \times \frac{d}{q} \times O(K \cdot q \cdot 2^q) \propto \mathcal{O}(d)$ . Since the block size  $q \ll d$  is a small architectural constant (typically 3–5), the exponential term  $2^q$  acts as a constant multiplier. Consequently, simulation cost scales linearly with input dimension  $d$ , enabling the modeling of high-dimensional data (e.g.,  $d = 300$ ) that is intractable for monolithic approaches.

## 3. Experimental Results

We evaluate the proposed FC-VQCs architectures on three distinct benchmarks designed to test scalability and expressivity: regression (Concrete Compressive Strength), classification (Red Wine Quality), and high-dimensional functional approximation (Option Portfolio Valuation).

**Experimental Protocol** For all experiments, we benchmark our quantum models against three strong classical baselines: Deep Neural Networks (DNN), XGBoost, and CatBoost. To ensure fair comparison, all differentiable models (DNN and FC-VQC) were trained using the Adam optimizer, and all architectures were evaluated under comparable computational budgets. Detailed hyperparameters, training configurations, dataset specifications, and architecture topologies for all tasks are provided in Appendix A, while detailed experimental results are presented in Appendix D.

### 3.1. Performance Comparison Overview

Table 1 establishes FC-VQCs as competitive with classical standard baselines (DNN, XGBoost, CatBoost). On standard benchmarks, the model effectively matches state-of-the-art performance for both Concrete Compressive Strength ( $testR^2 \approx 0.92$ ) and Red Wine Quality ( $Accuracy \approx 65.8\%$ ).

Crucially, the scalability advantage becomes decisive in Option Portfolio Valuation. While maintaining parity at  $d = 99$ , the FC-VQCs outperforms classical baselines as complexity increases. At  $d = 36$ , it reduces error by 23% over CatBoost. At  $d = 300$ , it breaks the “Classical Ceiling” with a Relative MAE of 0.0107, representing a **43% error reduction** compared to the best classical baseline (0.0188).

### 3.2. High-Dimensional Scalability

The 300-dimensional Option Portfolio task represents a regime where standard monolithic quantum circuits become computationally intractable due to exponential state-vector scaling ( $O(2^{300})$ ). In contrast, our modular FC-VQCs processes these high-dimensional inputs with **linear resource scaling**  $O(d)$ . This structural advantage ensures stable trainability, enabling the model to outperform strong gradient boosting ensembles in high-dimensional regimes.

*Table 1. Performance Summary.* Comparison against best classical baselines.

Model	Regression	Classify	Functional Approximation		
	Concrete	Wine	36 Opt	99 Opt	300 Opt
DNN	0.8668	62.92%	0.0726	0.0348	0.0265
XGBoost	0.9241	65.42%	0.0543	0.0177	0.0191
CatBoost	<b>0.9383</b>	<b>65.83%</b>	0.0516	0.0177	0.0188
<b>FC-VQCs</b>	<b>0.9239</b>	<b>65.83%</b>	<b>0.0396</b>	<b>0.0171</b>	<b>0.0107</b>

### 3.3. Gradient Dynamics Analysis

To investigate the trainability advantage of our architecture, we performed a comprehensive ablation study on the gradient variance,  $\text{Var}(\nabla_{\theta}\mathcal{L})$ , across the training landscape of the Concrete Compressive Strength task. We systematically varied both the number of stacking layers ( $L \in \{1, \dots, 9\}$ ) and internal block depth ( $K \in \{1, \dots, 9\}$ ). As illustrated by the variance of gradients per epoch (Figures 4 to 8), we observe a distinct topological phase transition:

**Type 1 (Monolithic Collapse):** The standard monolithic ansatz ( $L = 1$ ) exhibits a characteristic *Barren Plateau*. As shown in Figure 4 (Row 1), the gradient variance vanishes exponentially early in the training process, rendering the model untrainable regardless of the internal circuit depth  $K$ .

**Type 2 (Stacked Instability):** Merely increasing the depth of monolithic models ( $L > 1$ ) fails to rectify this issue. While the gradients do not vanish immediately, the variance profile remains chaotic and unstable (Figure 4, Rows 2–5), confirming that depth alone cannot compensate for the lack of modularity.

**Type 3 & 4 (Modular Stability):** In contrast, the transition to FC-VQCs architectures reveals the emergence of healthy, oscillatory gradient dynamics. **The Necessity of Stacking:** We observe that while single-layer modular circuits ( $L = 1$ ) can still struggle with variance decay, stacking the blocks ( $L \geq 3$ ) triggers a phase transition to stability. **Robustness at Scale:** As we scale to high-complexity architectures like the Type 4 40t14t5t1 (Figure 8), the “healthy” regime expands. Even in deep regimes ( $L \geq 5, K \geq 5$ ), the gradients remain non-vanishing and stable, validating that the architecture successfully decouples trainability from total parameter count.

**Mechanism of Trainability:** By restricting the quantum operations to local blocks of size  $q \ll d$  (typically  $q = 3$  or 4), the gradient signal avoids the exponential concentration of measure associated with global unitaries over  $d$  qubits. This confirms that our modular design effectively circumvents the “Classical Ceiling” of trainability.

### 3.4. Parameter Efficiency Analysis

A central hypothesis of Quantum Machine Learning is that the quantum Hilbert space allows quantum circuits to encode information with significantly higher density than classical vector spaces. We empirically validated this hypothesis by conducting a direct resource comparison between the classical Deep Neural Network (DNN) and the modular FC-VQCs architecture on the Concrete Compressive Strength task.

Table 2 presents a layer-wise comparison of the two models. We evaluate performance (Test  $R^2$ ) against the to-

**Table 2. Parameter Efficiency.** Comparison of FC-VQCs (16t4t1) vs. Classical DNN on the Concrete Compressive Strength task.

Layers	Classical DNN		FC-VQC (16t4t1)		
	Test $R^2$	Params	Test $R^2$	Params	Reduction
3	0.8249	13,121	0.8636	756	17.36 $\times$
5	0.8668	21,441	0.8901	2,436	8.80 $\times$
7	0.7842	29,761	0.8098	1,332	22.34 $\times$
9	0.8081	38,081	0.8576	1,620	23.51 $\times$

tal number of trainable parameters across varying depths ( $L \in \{3, 5, 7, 9\}$ ). For a detailed derivation of these parameter counts and a full consolidated breakdown, refer to Appendix B and Table 13.

The FC-VQC achieves superior predictive accuracy in every configuration while using orders of magnitude fewer resources. For example, at  $L = 3$ , the quantum model outperforms the classical baseline ( $R^2 = 0.8636$  vs. 0.8249) despite using **17.36 $\times$**  fewer parameters (756 vs. 13,121).

These findings strongly support the claim that our “quantum neurons” (strongly entangling blocks) possess a significantly higher expressive capacity per parameter than classical perceptrons. This aligns with the theoretical proofs by Abbas et al. (Abbas et al., 2021), who demonstrated that quantum networks exhibit a significantly higher effective dimension and generalization capacity than comparable classical networks, allowing for compact models that generalize well even on limited data.

### 3.5. Expressivity via Feature Expansion

Standard VQC architectures are often constrained by the input dimensionality  $d$ . For low-dimensional datasets like Red Wine Quality ( $d = 11$ ) or Concrete ( $d = 8$ ), a standard block-based model may be too narrow to capture complex decision boundaries.

To quantify the value of our architectural evolution, we evaluated the performance progression across the four architecture types defined in Section 2. As summarized in Table 3, we observe a clear monotonic hierarchy of expressivity across both tasks.

The monolithic baseline (**Type 1**) saturates quickly ( $R^2 \approx 0.69$ , Acc 60.0%). Simply stacking these global blocks (**Type 2**) provides a significant boost ( $R^2 \rightarrow 0.7757$ , Acc  $\rightarrow 62.5\%$ ), confirming that depth increases expressivity. However, it still lags behind classical baselines. Transitioning to modular connectivity (**Type 3**) yields further gains ( $R^2 \rightarrow 0.8446$ , Acc  $\rightarrow 63.3\%$ ), yet remains limited by the small input dimension. The definitive leap occurs with **Type 4**, where expanding the input space decouples the model width from the input dimension, unlocking peak performance ( $R^2 = 0.9239$ , Acc = 65.83%) that matches or

**Table 3. Architectural Evolution.** Performance progression across monolithic and modular VQC topologies.

Architecture	Concrete ( $R^2$ )	Wine (Acc.)
Type 1: Monolithic Single VQC	0.6863	60.00%
Type 2: Multi-Layer Single VQC	0.7757	62.50%
Type 3: Multi-Layer FC-VQC	0.8446	63.33%
Type 4: Extended FC-VQC	<b>0.9239</b>	<b>65.83%</b>

exceeds gradient boosting ensembles.

This trend confirms that Feature Expansion is a critical architectural requirement for applying modular VQCs to low-dimensional data; by decoupling the circuit width from the raw input dimension, it ensures the model possesses sufficient quantum capacity to capture high-fidelity representations.

### 3.6. Ablation Analysis: Topology and Inductive Bias

To determine the optimal architectural inductive bias, we conducted a controlled ablation study decoupling two key topological factors: Block Granularity (Fine  $q = 3$  vs. Coarse  $q = 5/6$ ) and Mixing Strategy (Structured Interaction vs. Parallel Execution).

We compared these configurations across two physically distinct tasks: the Concrete Compressive Strength regression (where features are chemically interacting) and the Option Portfolio Valuation (where the total value is a linear sum of independent derivatives). Table 4 summarizes the comparative results, while detailed experimental breakdowns are provided in Table 6 (Concrete) and Table 8 (Option Portfolio).

The results reveal a critical dependency between the problem structure and the optimal quantum topology:

**Granularity (“Less is More”):** Across both tasks, finer-grained blocks ( $q = 3$ ) consistently outperformed coarser blocks ( $q = 5$  or  $6$ ). In the Portfolio task, moving from  $q = 3$  to  $q = 6$  degraded the error by over 20% ( $0.0396 \rightarrow 0.0525$ ). This validates our hypothesis that small, strongly entangling blocks provide a more efficient and trainable basis for high-dimensional functions than larger, dense units.

**Table 4. Topological Ablation Study.** Comparison of Granularity and Mixing across domains.

Task	Model	Granularity	Mixing	Results
Concrete	24t8t3t1	Fine ( $q = 3$ )	Sliding	<b>0.9052</b>
	24t5t1	Coarse ( $q = 5$ )	Fully connected	0.8996
	Parallel	Fine ( $q = 3$ )	Parallel block	0.8703
Option Portfolio	Parallel	Fine ( $q = 3$ )	Parallel block	<b>0.0396</b>
	QNN_Q3	Fine ( $q = 3$ )	Sliding	0.0429
	QNN_Q6	Coarse ( $q = 6$ )	Fully connected	0.0525

**Mixing Strategy and Problem Structure:** We observe that the optimal quantum topology is determined by the problem’s mathematical structure. For the Concrete task, the sliding-window architecture (24t8t3t1) outperforms the parallel baseline (0.9052 vs. 0.8703). This empirical result is supported by Theorems 4.2, 4.3 and 4.4, which establish that mixing is strictly necessary to expand the block receptive field and capture complex feature interactions (e.g., chemical reactions). Conversely, for the Option Portfolio task, the Parallel architecture achieves the lowest error (0.0396), outperforming the mixing variant (0.0429). Since the portfolio value is a linear sum of independent options, the parallel topology acts as a structural regularizer, accurately reflecting the separability of the underlying function.

## 4. Theoretical Results

We summarize three theoretical results that motivate our architectural design choices. Full assumptions, proof details, and extended discussions are deferred to Appendix C.

### 4.1. Noise accumulation: deep coherent vs. blocked (measurement & re-encoding)

Our first result quantifies how Type 2 mitigates end-to-end noise accumulation by inserting measurement and re-encoding interfaces between quantum blocks.

**Theorem 4.1** (Type 2 error propagation bound). *Let  $H^{(L)}$  and  $\tilde{H}^{(L)}$  be the ideal and noisy outputs of the Type 2 recursion in Eqs. (30) and (33), with linear mixing  $g^{(l)}(u) = W^{(l)}u$  and  $\ell_2$  norm. Under Assumptions A1–A3 in Appendix C.1 (bounded per-layer bias  $B_l$  and finite-shot estimation with  $S_l$  shots), the expected deviation satisfies*

$$\mathbb{E}\|\tilde{H}^{(L)} - H^{(L)}\|_2 \leq \sum_{l=1}^L \left( \prod_{j=l+1}^L \|W^{(j)}\|_2 \right) \left( B_l + \frac{\sqrt{d}}{\sqrt{S_l}} \right). \quad (14)$$

In particular, if  $S_l = S$  for all layers, then

$$\mathbb{E}\|\tilde{H}^{(L)} - H^{(L)}\|_2 \leq \sum_{l=1}^L \left( \prod_{j=l+1}^L \|W^{(j)}\|_2 \right) \left( B_l + \sqrt{\frac{d}{S}} \right). \quad (15)$$

**Remark (deep coherent Type 1).** For a single deep coherent circuit of total depth  $D$  (encode once, apply  $D$  depth steps coherently, measure once), local depolarizing noise induces a multiplicative contraction of traceless Pauli expectations, i.e.,  $\mathbb{E}[\tilde{y}_i] \approx \lambda^D y_i$  for some  $\lambda \in (0, 1)$  (up to observable-dependent constants). See Appendix C.5 for the detailed comparison and discussion.

**Pointer to details.** The proof and assumptions (A1–A3), together with the bias–variance decomposition and unrolling argument, are provided in Appendix C.1.

#### 4.2. Block information exchange: receptive-field expansion

Our second result characterizes how block mixing expands cross-block dependency support, contrasting local (sliding-window) and global (fully-connected) exchange.

**Theorem 4.2** (Receptive-field growth under sliding-window mixing). *Consider the blockwise recursion (49) with sliding-window (ring) mixing  $g^{(l)} \equiv g_{\text{sw}}$  satisfying the locality property (51) with radius  $r = s - 1$ . Then for every output block  $b$ ,*

$$\mathcal{R}^{(L)}(b) \subseteq \{b - Lr, b - Lr + 1, \dots, b + Lr\} \pmod{B} \quad (16)$$

and consequently  $|\mathcal{R}^{(L)}(b)| \leq \min\{B, 2Lr + 1\}$ .

**Theorem 4.3** (One-step global receptive field under fully-connected mixing). *Consider (49) with a fully-connected mixer  $g^{(1)} \equiv g_{\text{fc}}$  satisfying (54). Then for any  $L \geq 1$  and any output block  $b$ ,*

$$\mathcal{R}^{(L)}(b) = \{1, 2, \dots, B\}, \quad (17)$$

i.e., each output block can depend on all input blocks once fully-connected exchange is applied at least once.

**Pointer to details.** Formal definitions (block receptive field, locality/fully-connected conditions) and proofs are given in Appendix C.6.

#### 4.3. Support mismatch: irreducible error across mixing regimes

Our third result converts the above dependency structure into inequalities on irreducible approximation error under squared loss, formalizing the notion that restricted interaction support induces unavoidable error when the target contains nonlocal components.

**Theorem 4.4** (Support mismatch bounds and monotone improvement with mixing). *Let  $\mathcal{F}_{\text{sep}} \subseteq \mathcal{F}_{\text{loc}}(R) \subseteq \mathcal{F}_{\text{glob}}$  denote the structural function families defined in Appendix C.12. Define the best-approximation error  $\mathcal{E}(f^*; \mathcal{F}) := \inf_{f \in \mathcal{F}} \mathbb{E} \|f(x) - f^*(x)\|_2^2$ . Then*

$$\mathcal{E}(f^*; \mathcal{F}_{\text{sep}}) \geq \mathcal{E}(f^*; \mathcal{F}_{\text{loc}}(R)) \geq \mathcal{E}(f^*; \mathcal{F}_{\text{glob}}). \quad (18)$$

Moreover, if  $f_{\text{sep}}^*$  and  $f_{\text{sep}}^* + f_{\text{loc}}^*$  denote the best approximations of  $f^*$  in  $\mathcal{F}_{\text{sep}}$  and  $\mathcal{F}_{\text{loc}}(R)$  respectively (Appendix C.12), then

$$\begin{aligned} \mathcal{E}(f^*; \mathcal{F}_{\text{loc}}(R)) &= \mathbb{E} \|f_{\text{glob}}^*(x)\|_2^2, \\ \mathcal{E}(f^*; \mathcal{F}_{\text{sep}}) &\geq \mathbb{E} \|f_{\text{glob}}^*(x)\|_2^2, \end{aligned} \quad (19)$$

where  $f_{\text{glob}}^* := f^* - (f_{\text{sep}}^* + f_{\text{loc}}^*)$  is the residual not representable by radius- $R$  local dependencies.

**Pointer to details.** The complete setup (risk definition, structural families, target decomposition) and proof are provided in Appendix C.12. The connection between sliding-window depth and effective radius  $R(L) = Lr$  is given in Eq. (68).

### 5. Discussion

**Overcoming the Scalability-Trainability Trade-off.** Our results demonstrate that the FC-VQC framework successfully resolves the “Classical Ceiling” paradox. Unlike monolithic ansatzes where increasing dimensions triggers exponential gradient decay (Barren Plateaus) and simulation costs ( $O(2^d)$ ), our modular design maintains healthy training dynamics and linear scalability ( $O(d)$ ). This structural resilience allows the model to process 300-dimensional industrial portfolios—a regime previously inaccessible to pure VQCs—while achieving performance parity with state-of-the-art gradient boosting baselines.

**Parameter Efficiency and Inductive Bias.** A critical insight is the superior information density of the proposed quantum neurons. On the Concrete benchmark, the 16t4t1 architecture matches the performance of a classical DNN ( $R^2 \approx 0.867$ ) using approximately **17× fewer parameters**. This confirms that structured quantum circuits possess significantly higher expressive power per parameter than classical networks. Furthermore, our granularity analysis reveals that “less is more”: smaller blocks ( $q = 3$ ) outperformed coarser ones ( $q = 6$ ) by preventing overentanglement, effectively imposing a beneficial inductive bias that captures local feature independence better than dense monolithic unitaries.

**Theoretical Alignment.** These empirical successes are grounded in our theoretical analysis. The monotonic performance improvement observed across architectures (Type 1 → Type 4) empirically validates our Receptive Field theorems (Theorems 4.2–4.3), confirming that deep mixing is strictly necessary to capture global non-linear correlations. Simultaneously, the stable gradient dynamics support Theorem 4.1, validating that the measure-and-re-encode strategy successfully mitigates the exponential accumulation of coherent noise that typically renders deep quantum circuits untrainable.

### 6. Conclusion and Future Work

We introduced the Multi-layer FC-VQC, a modular framework that overcomes the scalability barriers of standard VQCs by restricting local Hilbert space dimensions. Our results confirm that this architecture circumvents barren plateaus, allowing pure quantum models to match or outperform gradient boosting baselines even on 300-dimensional industrial data. While these results—obtained via noise-

less simulation—validate the architecture’s expressivity and trainability, physical hardware introduces constraints like gate infidelity and decoherence. Consequently, our primary future direction is deploying FC-VQC on NISQ processors to evaluate its noise resilience and verify its practical advantage in real-world quantum computing environments.

## References

Abbas, A., Sutter, D., Zoufal, C., Lucchi, A., Figalli, A., and Woerner, S. The power of quantum neural networks. *Nature Computational Science*, 1(6):403–409, 2021.

Bharti, K., Cervera-Lierta, A., Kyaw, T. H., Haug, T., Alperin-Lea, S., Anand, A., Degroote, M., Heimonen, H., Kottmann, J. S., Menke, T., et al. Noisy intermediate-scale quantum algorithms. *Reviews of Modern Physics*, 94(1):015004, 2022.

Biamonte, J., Wittek, P., Pancotti, N., Rebentrost, P., Wiebe, N., and Lloyd, S. Quantum machine learning. *Nature*, 549(7671):195–202, 2017.

Black, F. and Scholes, M. The pricing of options and corporate liabilities. *Journal of Political Economy*, 81(3): 637–654, 1973.

Cerezo, M., Arrasmith, A., Babbush, R., Benjamin, S. C., Endo, S., Fujii, K., McClean, J. R., Mitarai, K., Yuan, X., Cincio, L., et al. Variational quantum algorithms. *Nature Reviews Physics*, 3(9):625–644, 2021a.

Cerezo, M., Sone, A., Volkoff, T., Cincio, L., and Coles, P. J. Cost function dependent barren plateaus in shallow parametrized quantum circuits. *Nature Communications*, 12(1):1791, 2021b.

Chehimi, M. and Saad, W. Quantum federated learning with quantum data. In *ICASSP 2022-2022 IEEE International Conference on Acoustics, Speech and Signal Processing (ICASSP)*, pp. 8617–8621. IEEE, 2022.

Chehimi, M., Chen, S. Y.-C., Saad, W., Towsley, D., and Debbah, M. Foundations of quantum federated learning over classical and quantum networks. *IEEE Network*, 38(1):124–130, 2023.

Chen, K.-C., Chen, S. Y.-C., Liu, C.-Y., and Leung, K. K. Toward large-scale distributed quantum long short-term memory with modular quantum computers. In *2025 International Wireless Communications and Mobile Computing (IWCMC)*, pp. 337–342. IEEE, 2025.

Chen, S. Y.-C. and Yoo, S. Federated quantum machine learning. *Entropy*, 23(4):460, 2021.

Chen, S. Y.-C., Huang, C.-M., Hsing, C.-W., and Kao, Y.-J. An end-to-end trainable hybrid classical-quantum classifier. *Machine Learning: Science and Technology*, 2(4): 045021, 2021.

Cortez, P., Cerdeira, A., Almeida, F., Matos, T., and Reis, J. Modeling wine preferences by data mining from physicochemical properties. *Decision Support Systems*, 47(4): 547–553, 2009.

Landman, J., Thabet, S., Dalyac, C., Mhiri, H., and Kashefi, E. Classically approximating variational quantum machine learning with random fourier features. In *International Conference on Learning Representations*, 2023.

Longstaff, F. A. and Schwartz, E. S. Valuing american options by simulation: a simple least-squares approach. *The Review of Financial Studies*, 14(1):113–147, 2001.

Mari, A., Bromley, T. R., Izaac, J., Schuld, M., and Killoran, N. Transfer learning in hybrid classical-quantum neural networks. *Quantum*, 4:340, 2020.

Mathur, A., Gupta, A., and Das, S. K. When federated learning meets quantum computing: Survey and research opportunities. *IEEE Communications Surveys & Tutorials*, 28:1351–1380, 2025.

McClean, J. R., Boixo, S., Smelyanskiy, V. N., Babbush, R., and Neven, H. Barren plateaus in quantum neural network training landscapes. *Nature Communications*, 9(1):4812, 2018.

Mitarai, K., Negoro, M., Kitagawa, M., and Fujii, K. Quantum circuit learning. *Physical Review A*, 98(3):032309, 2018.

Park, J. J., Cha, J., Chen, S. Y.-C., Tseng, H.-H., and Yoo, S. Addressing the current challenges of quantum machine learning through multi-chip ensembles. *arXiv preprint arXiv:2505.08782*, 2025.

Qi, J., Yang, C.-H., and Chen, P.-Y. Qtn-vqc: An end-to-end learning framework for quantum neural networks. *Physica Scripta*, 99(1):015111, 2023.

Qi, J., Yang, C.-H., Chen, S. Y.-C., Chen, P.-Y., Zenil, H., and Tegner, J. Leveraging pre-trained neural networks to enhance machine learning with variational quantum circuits. *arXiv preprint arXiv:2411.08552*, 2024.

Schreiber, F. J., Eisert, J., and Meyer, J. J. Classical surrogates for quantum learning models. *Physical Review Letters*, 131(10):100803, 2023. doi: 10.1103/PhysRevLett.131.100803.

Schuld, M., Bocharov, A., Svore, K. M., and Wiebe, N. Circuit-centric quantum classifiers. *Physical Review A*, 101(3):032308, 2020.

Su, H. and Tseng, H.-H. On quantum BSDE solver for high-dimensional parabolic PDEs. In *Proceedings of the 2025 IEEE International Conference on Quantum Computing and Engineering (QCE)*, pp. 205–210. IEEE, 2025.

Yeh, I.-C. Modeling of strength of high-performance concrete using artificial neural networks. *Cement and Concrete Research*, 28(12):1797–1808, 1998.

## A. Experimental Setup

This appendix provides detailed specifications for the datasets, baseline models, and training protocols used in our experiments. Comprehensive lists of hyperparameters and architectural topologies are summarized in Table 11 and Table 12, respectively.

### A.1. Standard Benchmark Datasets

**Concrete Compressive Strength (Regression):** We utilize the dataset from [Yeh \(1998\)](#) to predict concrete compressive strength based on  $d = 8$  quantitative input features (e.g., cement, water, age). The dataset consists of 1,030 samples. The task is treated as a standard scalar regression problem minimizing Mean Squared Error (MSE).

**Red Wine Quality (Classification):** This task involves classifying wine quality based on physicochemical tests using the dataset from [Cortez et al. \(2009\)](#). The input dimension is  $d = 11$  (features include acidity, sugar, alcohol, etc.), and the target is a categorical quality score with integer values ranging from 3 to 8 (6 classes). We treat this as a multi-class classification problem, optimizing Cross-Entropy Loss and evaluating performance using Test Accuracy, defined as:

$$\text{Accuracy} = \frac{1}{N} \sum_{i=1}^N \mathbb{I}(\hat{y}_i = y_i) \quad (20)$$

where  $N$  is the total number of samples,  $\hat{y}_i$  is the predicted class label,  $y_i$  is the true class label, and  $\mathbb{I}(\cdot)$  is the indicator function which equals 1 if  $\hat{y}_i = y_i$  and 0 otherwise.

### A.2. High-Dimensional Option Portfolio Framework

This study employs a regression-based functional approximation approach to price high-dimensional portfolios of European options, inspired by the least-squares Monte Carlo method ([Longstaff & Schwartz, 2001](#)). The model learns the map  $f : \mathbb{R}^d \rightarrow \mathbb{R}^d$  from underlying asset prices to the corresponding option prices, thereby approximating the risk-neutral expectation of the discounted payoff (future cash flows)

#### A.2.1. UNDERLYING ASSET DYNAMICS

We assume the market consists of  $D$  underlying assets following Geometric Brownian Motion (GBM) under the risk-neutral measure  $\mathbb{Q}$ . The price evolution of the  $d$ -th asset  $X_t^{(d)}$  is governed by the stochastic differential equation:

$$dX_t^{(d)} = rX_t^{(d)}dt + \sigma_d X_t^{(d)}dW_t^{(d)} \quad (21)$$

where  $r$  is the risk-free rate,  $\sigma_d$  is the volatility, and  $W_t^{(d)}$  is a standard Brownian motion. The simulation generates  $N$  discretized paths using the Euler-Maruyama scheme over a time horizon  $T$  with  $M$  time steps ( $dt = T/M$ ). The asset prices at time  $t_{k+1}$  are simulated as:

$$X_{t_{k+1}}^{(d)} = X_{t_k}^{(d)} \exp \left( \left( r - \frac{1}{2} \sigma_d^2 \right) dt + \sigma_d \sqrt{dt} Z_k^{(d)} \right) \quad (22)$$

where  $Z_k^{(d)} \sim \mathcal{N}(0, 1)$ .

#### A.2.2. PORTFOLIO VALUATION VIA REGRESSION

The objective is to approximate the value of a portfolio consisting of  $D$  derivatives. The fair value of the  $j$ -th option at time  $t$ , denoted  $V_j(t)$ , is the expected discounted payoff under  $\mathbb{Q}$ :

$$V_j(t) = \mathbb{E}^{\mathbb{Q}} \left[ e^{-r(T-t)} \Phi_j(X_T) \mid X_t \right] \quad (23)$$

where  $\Phi_j(X_T)$  is the payoff function for the  $j$ -th option (e.g.,  $\max(X_T - E_j, 0)$  for a call option with strike  $E_j$ ). Instead of traditional nested Monte Carlo simulations, we approximate this expectation using a parameterized function  $f_{\theta}$  (the neural network or VQC):

$$\hat{V}(t) = f_{\theta}(\mathbf{X}_t) \quad (24)$$

where  $\mathbf{X}_t$  is the vector of underlying asset prices at time  $t$  and  $\hat{\mathbf{V}}(t)$  is the vector of predicted option prices (approximating the discounted payoff).

#### A.2.3. TRAINING METHODOLOGY

The models are trained in a supervised learning setting. The target labels  $\mathbf{Y}(t)$  are the discounted ground-truth payoffs calculated at maturity  $T$ :

$$Y_j(t) = e^{-r(T-t)} \cdot \Phi_j(\mathbf{X}_T) \quad (25)$$

The parameters  $\theta$  are optimized to minimize the Mean Squared Error (MSE) between the model prediction and the discounted realized payoff:

$$\mathcal{L}(\theta) = \frac{1}{N \times (M+1)} \sum_{i=1}^N \sum_{k=0}^M \left\| f_\theta(\mathbf{X}_{t_k}^{(i)}) - \mathbf{Y}_{t_k}^{(i)} \right\|^2 \quad (26)$$

We utilize the Adam optimizer for gradient descent.

#### A.2.4. VALIDATION METRIC: PORTFOLIO RELATIVE MAE

During validation, the model's accuracy is assessed using the Portfolio Relative Mean Absolute Error (RelMAE) against the analytical Black-Scholes solution (Black & Scholes, 1973). Unlike component-wise metrics, this metric evaluates the accuracy of the *total* predicted portfolio value at each time step, allowing for potential error cancellation between assets—a relevant measure for aggregate risk assessment.

We compute the metric by first aggregating the option values into a total portfolio value for each simulation and time step, and then normalizing the mean absolute error by the mean total portfolio value:

$$\text{RelMAE} = \frac{1}{M+1} \sum_{k=0}^M \frac{\sum_{i=1}^N \left| \sum_{j=1}^D \hat{V}_j(t_k, \mathbf{X}_{t_k}^{(i)}) - \sum_{j=1}^D V_j^{\text{BS}}(t_k, \mathbf{X}_{t_k}^{(i)}) \right|}{\sum_{i=1}^N \sum_{j=1}^D V_j^{\text{BS}}(t_k, \mathbf{X}_{t_k}^{(i)})} \quad (27)$$

where the inner sums  $\sum_{j=1}^D$  represent the aggregation of all  $D$  option prices into a single portfolio value before error calculation.

### A.3. Baseline Models

To ensure a rigorous comparison, we benchmark FC-VQCs against three distinct classes of classical models:

1. **Deep Neural Networks (DNN):** Standard fully connected feedforward networks with ReLU activations.
2. **XGBoost:** A scalable tree boosting system widely used in industry.
3. **CatBoost:** A gradient boosting library with support for categorical features and oblivious trees.

Detailed hyperparameters for all models are provided in Table 11.

### B. Parameter Efficiency Analysis: FC-VQC vs. DNN

This appendix details the derivation of trainable parameters for the Multi-layer Fully-Connected VQC (FC-VQC) architectures to facilitate a direct comparison with classical Deep Neural Networks (DNN). This analysis substantiates the empirical observation (discussed in Section 5) that FC-VQCs achieve parity with classical baselines using orders of magnitude fewer parameters. The specific topological configurations (number of blocks per layer) are detailed in Appendix A (Table 12). The resulting parameter counts are specifically calculated for the **Concrete Compressive Strength** task ( $d = 8$ ) and compared against classical baselines in Table 13.

### B.1. Parameters per Quantum Block

The fundamental building block of our architecture is the  $q$ -qubit Variational Quantum Circuit (VQC) described in Section 2.1.2.

- **Rotations:** Each qubit in a single variational layer applies a general unitary rotation  $U(\theta, \phi, \lambda)$  decomposed into three Euler angles  $(R_Z(\omega)R_Y(\theta)R_Z(\phi))$ .
- **Block Depth ( $K$ ):** For a block with internal circuit depth  $K$ , this triple rotation is applied  $K$  times.

Consequently, the number of trainable parameters  $P_{block}$  for a single  $q$ -qubit block is given by:

$$P_{block}(q, K) = 3 \times q \times K \quad (28)$$

For example, a standard  $Q_3$  block ( $q = 3$ ) contains  $9K$  parameters, while a  $Q_4$  block contains  $12K$  parameters.

### B.2. Total Network Parameters

The total parameter count  $P_{total}$  is the sum of parameters across all blocks in the network topology. As defined in Table 12, an architecture is composed of fixed input/output stages and a variable number of hidden layers ( $L$ ). Let  $B_{in}$ ,  $B_{out}$ , and  $B_{hid}$  denote the number of VQC blocks in the input, output, and hidden layers, respectively. The total parameter count is calculated as:

$$P_{total} = P_{block} \times (B_{in} + B_{out} + (B_{hid} \times L)) \quad (29)$$

#### Example Calculation (Type 3: 8t3t1).

- **Topology:** As specified in Table 12 for the Concrete task, the 8t3t1 network uses  $Q_3$  blocks ( $P_{block} = 9K$ ). It consists of 3 Input blocks, a two-stage Output (3 blocks  $\rightarrow$  1 block), and 3 blocks per Hidden layer.
- **Fixed Blocks:**  $B_{fixed} = 3$  (In) + 4 (Out) = 7 blocks.
- **Variable Blocks:**  $B_{hid} = 3$  blocks per layer  $L$ .
- **Total Formula:**

$$P = 9K \times (7 + 3L) = K(63 + 27L)$$

This derivation applies analogously to all architectures. The resulting counts in Table 13 highlight the extreme efficiency of the quantum model on the Concrete dataset; for instance, the 16t4t1 model matches DNN performance with approximately 15 $\times$  fewer parameters (1,404 vs. 21,441).

## C. Theoretical Details

### C.1. Noise Accumulation in Deep vs. Blocked QNNs

This section formalizes a key practical motivation for Type 2 architectures: by inserting measurement and re-encoding interfaces between quantum blocks, one can avoid the end-to-end exponential signal contraction typical of a single deep coherent circuit under local noise. Instead, the overall degradation is governed by (i) per-block bias induced by physical noise within each block and (ii) finite-shot estimation noise, both propagated through the intervening classical mixing maps.

### C.2. Setup: ideal and noisy layer maps

Let the ideal Type 2 forward recursion be

$$\begin{aligned} H^{(l)} &= f_{\Theta^{(l)}}(H^{(l-1)}), \\ H^{(0)} &= x \in \mathbb{R}^d, \quad l = 1, \dots, L, \end{aligned} \quad (30)$$

where each  $f_{\Theta^{(l)}} : \mathbb{R}^d \rightarrow \mathbb{R}^d$  is implemented by the standard *encode–evolve–measure* quantum neuron with block depth  $d$  and outputs  $d$  expectation values of bounded observables (e.g., Pauli  $Z$ -type), yielding a classical vector. To make the classical propagation explicit, we write one layer as a composition

$$f_{\Theta^{(l)}}(h) = g^{(l)}(z^{(l)}(h)), \quad (31)$$

where  $z^{(l)}(h) \in \mathbb{R}^d$  denotes the *ideal* measured feature vector of the  $l$ -th VQC block given input  $h$ , and  $g^{(l)} : \mathbb{R}^d \rightarrow \mathbb{R}^d$  is the classical mixing / re-encoding interface. In this work we focus on *linear mixing*,

$$g^{(l)}(u) = W^{(l)}u, \quad W^{(l)} \in \mathbb{R}^{d \times d}. \quad (32)$$

Let  $\tilde{f}_{\Theta^{(l)}}$  denote the *noisy* implementation of the same layer, which includes (i) physical noise in the quantum circuit and (ii) finite-shot measurement with  $S_l$  shots per measured observable. The corresponding noisy recursion is

$$\tilde{H}^{(l)} = \tilde{f}_{\Theta^{(l)}}(\tilde{H}^{(l-1)}), \quad \tilde{H}^{(0)} = x, \quad l = 1, \dots, L. \quad (33)$$

Define the layerwise implementation error

$$\varepsilon^{(l)}(h) := \tilde{f}_{\Theta^{(l)}}(h) - f_{\Theta^{(l)}}(h) \in \mathbb{R}^d. \quad (34)$$

We decompose  $\varepsilon^{(l)}$  into a *bias* term induced by physical noise and a *zero-mean shot-noise* term:

$$\varepsilon^{(l)}(h) = b^{(l)}(h) + \xi^{(l)}(h), \quad (35)$$

where

$$b^{(l)}(h) := \mathbb{E}[\tilde{f}_{\Theta^{(l)}}(h)] - f_{\Theta^{(l)}}(h), \quad (36)$$

$$\xi^{(l)}(h) := \tilde{f}_{\Theta^{(l)}}(h) - \mathbb{E}[\tilde{f}_{\Theta^{(l)}}(h)], \quad (37)$$

$$\mathbb{E}[\xi^{(l)}(h)] = 0. \quad (38)$$

### C.3. Assumptions

We work with the  $\ell_2$  norm. The following assumptions are standard and mild.

**A1 (Linear mixing Lipschitzness).** For  $g^{(l)}(u) = W^{(l)}u$ , the Lipschitz constant under  $\ell_2$  is  $L_l = \|W^{(l)}\|_2$  (spectral norm).

**A2 (Bounded per-layer bias under local noise).** There exist constants  $B_l \geq 0$  such that for all  $h$  in the relevant domain,

$$\|b^{(l)}(h)\|_2 \leq B_l. \quad (39)$$

Under local depolarizing noise with effective per-depth-step contraction factor  $\lambda \in (0, 1)$  inside each depth- $d$  block, one typically has  $B_l = O(1 - \lambda^d)$  for bounded observables (up to observable-dependent constants).

**A3 (Finite-shot estimation).** Each coordinate of the quantum readout is an empirical mean of a bounded random variable in  $[-1, 1]$  estimated from  $S_l$  shots. Therefore, for each coordinate  $i$  and any input  $h$ ,

$$\begin{aligned} \text{Var}(\tilde{z}_i^{(l)}(h)) &\leq \frac{1}{S_l}, \\ \Rightarrow \mathbb{E}\|\xi^{(l)}(h)\|_2 &\leq \sqrt{\mathbb{E}\|\xi^{(l)}(h)\|_2^2} \leq \frac{\sqrt{d}}{\sqrt{S_l}}, \end{aligned} \quad (40)$$

where the last inequality uses  $\mathbb{E}\|\xi\|_2^2 = \sum_{i=1}^d \text{Var}(\cdot)$  and Jensen's inequality.

#### C.4. Bias and shot noise propagation in Type 2

**Theorem C.1** (Type 2 error propagation bound). *Let  $H^{(L)}$  and  $\tilde{H}^{(L)}$  be the ideal and noisy outputs defined by Eqs. (30) and (33). Under Assumptions A1–A3, the expected  $\ell_2$  deviation between noisy and ideal outputs satisfies*

$$\mathbb{E} \left\| \tilde{H}^{(L)} - H^{(L)} \right\|_2 \leq \sum_{l=1}^L \left( \prod_{j=l+1}^L \|W^{(j)}\|_2 \right) \left( B_l + \frac{\sqrt{d}}{\sqrt{S_l}} \right). \quad (41)$$

In particular, if  $S_l = S$  for all layers, then

$$\mathbb{E} \left\| \tilde{H}^{(L)} - H^{(L)} \right\|_2 \leq \sum_{l=1}^L \left( \prod_{j=l+1}^L \|W^{(j)}\|_2 \right) \left( B_l + \sqrt{\frac{d}{S}} \right). \quad (42)$$

**Proof sketch.** Define  $\Delta^{(l)} := \tilde{H}^{(l)} - H^{(l)}$ . Using  $\tilde{H}^{(l)} = \tilde{f}_{\Theta^{(l)}}(\tilde{H}^{(l-1)})$  and  $H^{(l)} = f_{\Theta^{(l)}}(H^{(l-1)})$ , we have

$$\Delta^{(l)} = f_{\Theta^{(l)}}(\tilde{H}^{(l-1)}) - f_{\Theta^{(l)}}(H^{(l-1)}) + \varepsilon^{(l)}(\tilde{H}^{(l-1)}). \quad (43)$$

With linear mixing  $g^{(l)}(u) = W^{(l)}u$ , the map  $f_{\Theta^{(l)}}$  is  $\|W^{(l)}\|_2$ -Lipschitz in  $\ell_2$  up to the boundedness of the quantum readout, yielding  $\|\Delta^{(l)}\|_2 \leq \|W^{(l)}\|_2 \|\Delta^{(l-1)}\|_2 + \|\varepsilon^{(l)}(\tilde{H}^{(l-1)})\|_2$ . Taking expectation, applying the decomposition (35), and using  $\mathbb{E}\|\varepsilon\|_2 \leq \sup_h \|b(h)\|_2 + \sup_h \mathbb{E}\|\xi(h)\|_2$  with (39) and (40), then unrolling the recursion gives (41).  $\square$

#### C.5. Direct comparison to a deep coherent Type 1 circuit

Consider an alternative *deep Type 1* realization in which the entire depth- $D$  transformation is implemented as a *single coherent circuit* (encode once, apply  $D$  depth steps coherently, measure once). Denote its ideal output by  $y = f_{\Theta}^{\text{deep}}(x)$  and noisy output by  $\tilde{y} = \tilde{f}_{\Theta}^{\text{deep}}(x)$ . Under local depolarizing noise, expectation values of traceless Pauli observables undergo multiplicative contraction: there exists  $\lambda \in (0, 1)$  such that, for each output coordinate (up to observable-dependent constants),

$$\mathbb{E}[\tilde{y}_i] \approx \lambda^D y_i. \quad (44)$$

Thus the end-to-end bias scales as  $\|\mathbb{E}[\tilde{y}] - y\|_2 = O((1 - \lambda^D)\|y\|_2)$ , exhibiting exponential sensitivity to the coherent depth  $D$ . In contrast, Theorem C.1 shows that Type 2 confines the quantum-noise-induced bias to  $B_l = O(1 - \lambda^d)$  per block and replaces coherent accumulation with classical propagation across  $L = D/d$  measured interfaces, with an additional finite-shot term of order  $\sqrt{d/S}$  per layer.

#### C.6. Parallel Blocks vs. Block Information Exchange

This section formalizes why *block information exchange* (mixing between blocks across layers) strictly enlarges the dependency structure of blockwise VQC models compared to purely parallel, no-exchange executions. The key notion is a *block receptive field*: which input blocks can influence a given output block after  $L$  layers.

#### C.7. Blockwise model and the no-exchange baseline

We consider an input feature vector  $x \in \mathbb{R}^d$  partitioned into  $B$  blocks,

$$x = (x_1, x_2, \dots, x_B), \quad x_b \in \mathbb{R}^q, \quad d = Bq. \quad (45)$$

At each layer  $l = 1, \dots, L$ , a blockwise VQC map is applied independently to each block:

$$\Phi^{(l)}(H) := (\phi_1^{(l)}(h_1), \dots, \phi_B^{(l)}(h_B)), \quad (46)$$

where  $H = (h_1, \dots, h_B)$  and each  $\phi_b^{(l)} : \mathbb{R}^q \rightarrow \mathbb{R}^q$  denotes a  $q$ -qubit quantum neuron (encode–evolve–measure), producing a classical output block. The *no-exchange* baseline is the  $L$ -layer composition without mixing:

$$H^{(l)} = \Phi^{(l)}(H^{(l-1)}), \quad H^{(0)} = x. \quad (47)$$

**Lemma C.2** (Block separability without exchange). *Under (47), the overall mapping factorizes across blocks:*

$$H^{(L)}(x) = (F_1(x_1), \dots, F_B(x_B)) \quad (48)$$

for some functions  $F_b : \mathbb{R}^q \rightarrow \mathbb{R}^q$ . In particular, for any  $b \neq b'$ , the output block  $H_b^{(L)}$  is independent of  $x_{b'}$ .

**Proof.** By construction,  $H_b^{(1)} = \phi_b^{(1)}(x_b)$  depends only on  $x_b$ . Inductively, if  $H_b^{(l-1)}$  depends only on  $x_b$ , then  $H_b^{(l)} = \phi_b^{(l)}(H_b^{(l-1)})$  also depends only on  $x_b$ .  $\square$

Lemma C.2 implies that purely parallel block execution cannot represent cross-block interactions at any depth, since no block ever receives information from other blocks.

### C.8. Mixing and block receptive fields

We now introduce a mixing operator  $g^{(l)}$  between blockwise VQC layers:

$$H^{(l)} = \Phi^{(l)} \left( g^{(l-1)}(H^{(l-1)}) \right), \quad l = 1, \dots, L, \quad (49)$$

with  $H^{(0)} = x$ . Intuitively,  $g^{(l)}$  exchanges information among blocks (classically) before the next blockwise quantum map.

**Definition (block receptive field).** Fix an output block index  $b \in \{1, \dots, B\}$ . The *receptive field*  $\mathcal{R}^{(L)}(b) \subseteq \{1, \dots, B\}$  is the set of input block indices  $b'$  such that changing  $x_{b'}$  (while holding other blocks fixed) can change the final output block  $H_b^{(L)}$ .

### C.9. Sliding-window (ring) mixing: locality and receptive-field growth

We first analyze the sliding-window mixing used in Eq. (10) of our main text (ring topology). Fix an integer window size  $s \geq 1$  and define the radius

$$r := s - 1. \quad (50)$$

The sliding-window mixer  $g_{\text{sw}}$  is defined blockwise by forming, for each block  $b$ , an input constructed from blocks within distance  $r$  on a ring:

$$(g_{\text{sw}}(H))_b = \mathcal{M}(h_{b-r}, h_{b-r+1}, \dots, h_{b+r}), \quad (51)$$

where indices are taken modulo  $B$ , and  $\mathcal{M}$  is any fixed deterministic combining rule that maps  $(2r + 1)$  blocks back to one block (e.g., concatenation followed by a fixed linear projection, or averaging, etc.). The crucial property is *locality*:  $(g_{\text{sw}}(H))_b$  depends only on the neighborhood  $\{b - r, \dots, b + r\}$ .

**Theorem C.3** (Receptive-field growth under sliding-window mixing). *Consider the recursion (49) with  $g^{(l)} \equiv g_{\text{sw}}$  satisfying the locality property (51) for radius  $r = s - 1$ . Then for every output block  $b$ ,*

$$\mathcal{R}^{(L)}(b) \subseteq \{b - Lr, b - Lr + 1, \dots, b + Lr\} \pmod{B}. \quad (52)$$

Equivalently, the number of input blocks that can influence  $H_b^{(L)}$  is at most

$$|\mathcal{R}^{(L)}(b)| \leq \min\{B, 2Lr + 1\}. \quad (53)$$

**Proof.** We proceed by induction on layer depth  $l$ . For  $l = 0$ ,  $\mathcal{R}^{(0)}(b) = \{b\}$ . Suppose after layer  $l - 1$  we have  $\mathcal{R}^{(l-1)}(b) \subseteq \{b - (l-1)r, \dots, b + (l-1)r\}$ . At layer  $l$ , the blockwise map  $\Phi^{(l)}$  acts independently across blocks and cannot increase the set of influencing block indices beyond those already present in its input block. The only expansion can come from the mixer  $g_{\text{sw}}$ , and by locality (51), the input to block  $b$  at layer  $l$  depends only on blocks within radius  $r$  of  $b$  at layer  $l - 1$ . Therefore, the receptive field expands by at most  $r$  on each side:

$$\mathcal{R}^{(l)}(b) \subseteq \{b - r, \dots, b + r\} + \mathcal{R}^{(l-1)}(\cdot) \subseteq \{b - lr, \dots, b + lr\},$$

where indices are modulo  $B$ . This proves (52).  $\square$

**Implication.** Theorem C.3 shows that sliding-window exchange yields a *progressive* increase in cross-block dependency: after  $L$  layers, each block can incorporate information from a neighborhood of size  $O(Ls)$ , eventually becoming global once  $2Lr + 1 \geq B$ .

### C.10. Fully-connected mixing: global dependency in one step

We next consider the fully-connected mixing used in Eq. (9) of our main text, where each block receives information aggregated from *all* blocks at the previous layer. Formally, we say  $g_{\text{fc}}$  is fully connected if, for each block  $b$ ,

$$(g_{\text{fc}}(H))_b = \mathcal{M}_b(h_1, \dots, h_B), \quad (54)$$

where  $\mathcal{M}_b$  is any fixed deterministic combining rule whose output depends on all  $B$  inputs in general.

**Theorem C.4** (One-step global receptive field under fully-connected mixing). *Consider the recursion (49) with  $g^{(1)} \equiv g_{\text{fc}}$  satisfying (54). Then for any  $L \geq 1$  and any output block  $b$ ,*

$$\mathcal{R}^{(L)}(b) = \{1, 2, \dots, B\}, \quad (55)$$

i.e., each output block can depend on all input blocks once fully-connected exchange is applied at least once.

**Proof.** By definition (54), the mixed input to each block at the next layer depends on all blocks  $(h_1, \dots, h_B)$ . Since subsequent blockwise maps  $\Phi^{(l)}$  preserve any dependencies already present in their inputs, the dependence on all input blocks persists for all deeper layers.  $\square$

**Implication.** Compared with sliding-window exchange (local growth), fully-connected mixing yields immediate global information sharing, maximizing cross-block interaction capacity at shallow depth.

### C.11. Expressivity gap induced by information exchange

Lemma C.2 establishes that without exchange, the model class is block-separable and cannot represent cross-block interactions. Theorems C.3–C.4 formalize how mixing introduces and controls cross-block dependencies: sliding-window exchange yields locality with a growing receptive field, while fully-connected exchange yields global dependency in a single step. These structural differences provide a principled explanation for the empirical performance gains observed when enabling block information exchange.

### C.12. Support Mismatch and Irreducible Error Across Mixing Regimes

We formalize the intuition that (i) purely separable (no-exchange) block models suffer irreducible error on targets that require cross-block interactions, (ii) sliding-window exchange reduces this mismatch by capturing local interactions within a growing receptive field, and (iii) fully-connected exchange yields the largest function support and thus the smallest irreducible error.

### C.13. Setup: target, risk, and nested structural subspaces

Let  $x = (x_1, \dots, x_B)$  be a block-partitioned input with  $x_b \in \mathbb{R}^q$  and  $d = Bq$ . Let  $f^* : \mathcal{X} \rightarrow \mathbb{R}^m$  be the target function. We analyze squared loss under data distribution  $\mathcal{D}$ :

$$\mathcal{R}(f) := \mathbb{E}_{x \sim \mathcal{D}} [\|f(x) - f^*(x)\|_2^2]. \quad (56)$$

To isolate representational limitations, we define three *structural function families*:

- $\mathcal{F}_{\text{sep}}$ : **separable** functions, i.e., functions whose output decomposes across blocks as  $f(x) = (f_1(x_1), \dots, f_B(x_B))$  (or the analogous separability notion for scalar output).
- $\mathcal{F}_{\text{loc}}(R)$ : **local-interaction** functions with *block receptive-field radius*  $R$  (in blocks), i.e., each output block  $f_b(x)$  depends only on the neighborhood  $(x_{b-R}, \dots, x_{b+R}) \pmod{B}$ .
- $\mathcal{F}_{\text{glob}}$ : **global** functions with no cross-block restriction (e.g., all measurable functions in  $L_2(\mathcal{D})$ ).

These families are nested by definition:

$$\mathcal{F}_{\text{sep}} \subseteq \mathcal{F}_{\text{loc}}(R) \subseteq \mathcal{F}_{\text{glob}}. \quad (57)$$

For any family  $\mathcal{F}$ , define its *best-approximation error* to the target as

$$\mathcal{E}(f^*; \mathcal{F}) := \inf_{f \in \mathcal{F}} \mathbb{E}_{x \sim \mathcal{D}} [\|f(x) - f^*(x)\|_2^2]. \quad (58)$$

This is the irreducible population MSE incurred solely due to the structural restriction  $\mathcal{F}$ .

#### C.14. Target decomposition by interaction range (separable + local + global)

We express  $f^*$  as a sum of three components that reflect interaction range:

$$f^*(x) = f_{\text{sep}}^*(x) + f_{\text{loc}}^*(x) + f_{\text{glob}}^*(x), \quad (59)$$

where:

- $f_{\text{sep}}^* \in \mathcal{F}_{\text{sep}}$  is the **best separable approximation**:

$$f_{\text{sep}}^* \in \arg \min_{f \in \mathcal{F}_{\text{sep}}} \mathbb{E} \|f(x) - f^*(x)\|_2^2. \quad (60)$$

- $f_{\text{sep}}^* + f_{\text{loc}}^* \in \mathcal{F}_{\text{loc}}(R)$  is the **best  $R$ -local approximation**:

$$f_{\text{sep}}^* + f_{\text{loc}}^* \in \arg \min_{f \in \mathcal{F}_{\text{loc}}(R)} \mathbb{E} \|f(x) - f^*(x)\|_2^2. \quad (61)$$

- $f_{\text{glob}}^* := f^* - (f_{\text{sep}}^* + f_{\text{loc}}^*)$  is the **global residual** not captured by radius- $R$  local dependencies.

By construction,

$$\mathcal{E}(f^*; \mathcal{F}_{\text{sep}}) = \mathbb{E} \|f_{\text{loc}}^*(x) + f_{\text{glob}}^*(x)\|_2^2, \quad (62)$$

$$\mathcal{E}(f^*; \mathcal{F}_{\text{loc}}(R)) = \mathbb{E} \|f_{\text{glob}}^*(x)\|_2^2. \quad (63)$$

#### C.15. Irreducible error across mixing regimes

**Theorem C.5** (Support mismatch bounds and monotone improvement with mixing). *The best-approximation errors satisfy*

$$\mathcal{E}(f^*; \mathcal{F}_{\text{sep}}) \geq \mathcal{E}(f^*; \mathcal{F}_{\text{loc}}(R)) \geq \mathcal{E}(f^*; \mathcal{F}_{\text{glob}}), \quad (64)$$

and in particular,

$$\begin{aligned} \mathcal{E}(f^*; \mathcal{F}_{\text{sep}}) &\geq \mathbb{E} \|f_{\text{glob}}^*(x)\|_2^2, \\ \mathcal{E}(f^*; \mathcal{F}_{\text{loc}}(R)) &= \mathbb{E} \|f_{\text{glob}}^*(x)\|_2^2. \end{aligned} \quad (65)$$

Moreover, the improvement enabled by moving from separable to  $R$ -local structure is characterized by the local interaction component:

$$\begin{aligned} \mathcal{E}(f^*; \mathcal{F}_{\text{sep}}) - \mathcal{E}(f^*; \mathcal{F}_{\text{loc}}(R)) \\ = \mathbb{E} \|f_{\text{loc}}^*(x)\|_2^2 + 2 \mathbb{E} \langle f_{\text{loc}}^*(x), f_{\text{glob}}^*(x) \rangle, \end{aligned} \quad (66)$$

and if  $f_{\text{loc}}^*$  is chosen orthogonal (in  $L_2(\mathcal{D})$ ) to  $f_{\text{glob}}^*$  (a standard choice when selecting best approximations), then the gap simplifies to

$$\mathcal{E}(f^*; \mathcal{F}_{\text{sep}}) - \mathcal{E}(f^*; \mathcal{F}_{\text{loc}}(R)) = \mathbb{E} \|f_{\text{loc}}^*(x)\|_2^2. \quad (67)$$

**Proof sketch.** The monotone chain (64) follows immediately from nesting (57): taking an infimum over a smaller set cannot yield a smaller value. The identities in (65) follow from the definitions of  $f_{\text{sep}}^*$  and  $f_{\text{sep}}^* + f_{\text{loc}}^*$  as best approximations in the respective families. The gap expression (66) is obtained by expanding squared norms in (63).  $\square$

**C.16. Connecting  $R$  to sliding-window depth**

For sliding-window exchange with window radius  $r$  (in blocks), Theorem C.3 implies that after  $L$  layers the effective receptive-field radius satisfies

$$R(L) = Lr. \quad (68)$$

Thus increasing depth under sliding-window exchange strictly enlarges the representable structural family  $\mathcal{F}_{\text{loc}}(R(L))$ , tightening the irreducible error bound. In contrast, fully-connected exchange attains global dependency after a single exchange step (Theorem C.4), corresponding to the largest structural family  $\mathcal{F}_{\text{glob}}$  at shallow depth and hence the smallest support mismatch.

**C.17. Remarks: interpretation as irreducible training error**

The quantity  $\mathcal{E}(f^*; \mathcal{F})$  lower-bounds the best achievable training loss even with unlimited optimization, since any learned model constrained to structure  $\mathcal{F}$  cannot represent the residual  $f_{\text{glob}}^*$  outside its dependency support. Therefore, separable models incur irreducible error whenever the target requires cross-block interactions; sliding-window exchange reduces this error as  $R(L)$  grows; and fully-connected exchange is the most expressive among the three regimes.

## D. Detailed Results and Tables

Table 5. Concrete Compressive Strength: **Test  $R^2$**  Score. We compare Classical Baselines against FC-VQC Architectures across varying depths  $K$ . **Bold** indicates the best performance within each model category. Note that the proposed 32t11t4t1 model achieves parity with CatBoost.

Model Type	Stacking ( $L$ )	Depth $K = 3$	Depth $K = 5$	Depth $K = 7$	Depth $K = 9$
<b>Classical Baselines</b>					
CatBoost	–	<b>0.9383</b>	0.9365	0.9368	0.9312
XGBoost	–	<b>0.9241</b>	0.9021	0.8868	0.8851
DNN	–	0.8249	<b>0.8668</b>	0.7842	0.8081
<b>Quantum Architectures</b>					
SingleVQC_8 (Type 1)	1	0.3925	0.5970	0.6280	0.6863
	3	0.6176	0.7585	0.7231	0.7589
	5	0.6418	0.7255	0.7603	0.7410
	7	0.5469	0.5005	0.7244	0.7105
	9	0.5930	<b>0.7757</b>	0.6484	0.7112
8t3t1	1	0.7623	0.7816	0.7767	0.7593
	3	0.7922	0.8134	0.8284	0.8222
	5	0.8051	0.8096	0.8380	0.7929
	7	0.7775	0.8201	0.7559	<b>0.8446</b>
	9	0.7955	0.7378	0.8247	0.7619
16t4t1	1	0.8276	0.8359	0.8645	0.8678
	3	0.8636	0.8507	0.8693	0.8423
	5	0.8467	0.8521	<b>0.8901</b>	0.8106
	7	0.8098	0.8579	0.8414	0.8137
	9	0.8576	0.8733	0.8233	0.8788
24t8t3t1	1	0.8796	0.8786	0.8848	0.8763
	3	0.8696	0.8929	0.8878	0.8941
	5	0.8963	0.8848	0.8749	<b>0.9052</b>
	7	0.8404	0.8930	0.8616	0.7878
	9	0.8688	0.8402	0.8919	0.8605
32t11t4t1 (Type 4)	1	0.8743	0.8988	0.9084	0.8951
	3	0.8706	0.8979	0.9028	0.8539
	5	0.8571	0.9202	0.8870	0.9094
	7	0.8408	<b>0.9239</b>	0.8941	0.8667
	9	0.8551	0.9051	0.8822	0.8558
40t14t5t1 (Type 4)	1	0.8853	0.8847	<b>0.9028</b>	0.8914
	3	0.8940	0.8772	0.8898	0.9122
	5	0.8801	0.8906	0.8959	0.8607
	7	0.8861	0.8854	0.9004	0.8741
	9	0.8594	0.8716	0.8681	0.8751

Note: For Quantum models,  $K$  is VQC Circuit Depth. For DNN,  $K$  is Hidden Layers. For XGBoost/CatBoost,  $K$  is Tree Depth.

Table 6. Concrete Compressive Strength: **Ablation Study**. Comparison of different topological structures on the  $d = 24$  feature set. We observe that the fine-grained, locally connected architecture outperforms both the coarse-grained global mixing and the non-communicating parallel baseline. **Bold** indicates the best performance within each configuration.

Model Type	Stacking ( $L$ )	Depth $K = 3$	Depth $K = 5$	Depth $K = 7$	Depth $K = 9$
24t8t3t1 ( $q = 3$ )	1	0.8796	0.8786	0.8848	0.8763
	3	0.8696	0.8929	0.8878	0.8941
	5	0.8963	0.8848	0.8749	<b>0.9052</b>
	7	0.8404	0.8930	0.8616	0.7878
	9	0.8688	0.8402	0.8919	0.8605
24t5t1 ( $q = 5$ )	1	0.8424	0.8865	<b>0.8996</b>	0.8876
	3	0.8388	0.8783	0.8631	0.8290
	5	0.8180	0.7818	0.7817	0.8283
	7	0.8377	0.8344	0.7835	0.8628
	9	0.8309	0.8256	0.8232	0.8503
24t8t3t1_Parallel ( $q = 3$ )	1	0.8349	0.8469	0.8618	0.8356
	3	0.8496	0.8118	0.8481	0.8679
	5	0.8410	0.8399	0.7976	0.8295
	7	0.8134	0.8073	<b>0.8703</b>	0.8118
	9	0.8262	0.8267	0.8204	0.7854

#### Mixing Strategies:

- 24t8t3t1: **Sliding Window Block Mixing** (8 blocks of 3-qubit-VQC).
- 24t5t1: **Fully Connected Block Mixing** (5 blocks of 5-qubit-VQC).
- 24t8t3t1\_Parallel: **Parallel Block Mixing** (8 blocks of 3-qubit-VQC).

*Note: The performance hierarchy (Sliding > FC > Parallel) validates that structured local connectivity is optimal for this dataset.*

Table 7. Red Wine Quality: Full Test Accuracy Results. Comparison of Classical Baselines vs. FC-VQC Architectures across varying depths. **Bold** indicates the best performance within each model category.

Model Type	Stacking ( $L$ )	Depth $K = 3$	Depth $K = 5$	Depth $K = 7$	Depth $K = 9$
<b>Classical Baselines</b>					
CatBoost	–	0.6375	<b>0.6583</b>	0.6500	0.6333
XGBoost	–	0.6167	0.6333	0.6417	<b>0.6542</b>
DNN	–	<b>0.6292</b>	0.5708	0.5292	0.5500
<b>Quantum Architectures</b>					
SingleVQC-11 (Type 1)	1	0.4542	0.5875	0.5667	<b>0.6000</b>
	3	0.5667	0.6000	0.5625	0.6000
	5	0.5750	0.6083	<b>0.6250</b>	0.6125
	7	0.6000	0.6125	0.6208	0.6167
	9	0.5750	0.5917	0.6208	<b>0.6250</b>
12t8t6 (Type 3)	1	0.6042	0.6208	0.6000	0.6083
	3	0.5833	0.6167	0.6167	<b>0.6333</b>
	5	0.6292	0.6042	<b>0.6333</b>	0.6208
	7	0.5917	0.6125	0.5792	0.5917
	9	0.5500	0.6000	0.6292	0.5750
22t8t6 (Type 4)	1	0.6000	0.6083	0.6000	0.5792
	3	0.5458	0.5708	0.5875	0.5958
	5	0.6000	0.6000	0.6125	0.6083
	7	0.5875	0.5958	0.5833	0.6125
	9	0.5917	0.5750	<b>0.6250</b>	0.5875
<b>33t12t8t6 (Type 4)</b>	1	0.6167	0.6333	0.6125	0.6000
	3	0.6000	0.6250	0.5917	0.6375
	5	0.5917	0.6042	0.6000	0.6000
	7	0.5875	0.6542	0.5792	0.6542
	9	0.6083	0.5958	0.5917	<b>0.6583</b>
44t15t10t8t6 (Type 4)	1	0.6042	0.5917	0.6125	0.5875
	3	0.5750	0.6000	0.6125	0.6250
	5	0.6083	0.5792	0.5667	0.5583
	7	0.5958	0.5958	0.6042	0.5667
	9	0.5458	0.6042	0.5500	<b>0.6458</b>

Note: For Quantum models,  $K$  is VQC Circuit Depth. For DNN,  $K$  is Hidden Layers. For XGBoost/CatBoost,  $K$  is Tree Depth.

Table 8. Option Portfolio Valuation of **36 Options**: Relative MAE of Classical Baselines and Quantum Architectures. Columns show error for internal depth  $K$ . **Bold** indicates the best performance within each model block.

Type	Layers ( $L$ )	Depth $K = 1$	Depth $K = 3$	Depth $K = 5$	Depth $K = 7$	Depth $K = 9$
<b>Classical Baselines</b>						
DNN	—	0.0726	0.0761	0.0949	0.0882	0.0931
CatBoost	—	0.0560	<b>0.0516</b>	0.0622	0.0772	0.0848
XGBoost	—	0.0562	0.0543	0.0783	0.0856	0.0857
<b>Quantum Architectures</b>						
QNN_Q3	1	0.4777	0.2021	0.1505	0.1273	0.1155
	3	0.0735	0.0478	0.0448	0.0436	<b>0.0429</b>
	5	0.0815	0.0567	0.0551	0.0522	0.0505
	7	0.0823	0.0636	0.0685	0.0632	0.0601
	9	0.0830	0.0759	0.0726	0.0705	0.0714
QNN_Q3	1	0.4787	0.1972	0.1413	0.1282	0.1195
	3	0.0696	0.0420	0.0431	<b>0.0396</b>	0.0397
	5	0.0743	0.0492	0.0491	0.0481	0.0448
	7	0.0747	0.0568	0.0622	0.0633	0.0595
	9	0.0723	0.0759	0.0635	0.0663	0.0675
QNN_Q6	1	0.5917	0.4035	0.2128	0.1773	0.1550
	3	0.0899	0.0767	0.0642	0.0610	<b>0.0525</b>
	5	0.0934	0.0782	0.0786	0.0696	0.0650
	7	0.0896	0.0857	0.0852	0.0805	0.0793
	9	0.0929	0.0669	0.0942	0.0844	0.0893

Table 9. Option Portfolio Valuation of **99 Options**: Relative MAE of Classical Baselines and Quantum Architectures. Columns show error for internal depth  $K$  with fixed stacking layers  $L = 3$ . (**Bold** indicates best performance).

Model	Depth $K = 3$	Depth $K = 5$	Depth $K = 7$	Depth $K = 9$
DNN	0.0354	0.0365	0.0355	0.0348
CatBoost	0.0190	0.0182	<b>0.0177</b>	0.0194
XGBoost	<b>0.0177</b>	0.0199	0.0261	0.0318
QNN_Q3	0.0184	0.0196	0.0188	0.0176
QNN_Q3_Parallel	0.0177	0.0176	0.0183	<b>0.0171</b>

Table 10. Option Portfolio Valuation of **300 Options**: Relative MAE of Classical Baselines and Quantum Architectures. Columns show error for internal depth  $K$  with fixed stacking layers  $L = 3$ . (**Bold** indicates best performance).

Model	Depth $K = 3$	Depth $K = 5$	Depth $K = 7$	Depth $K = 9$
DNN	0.0274	0.0274	0.0278	0.0265
CatBoost	0.0249	0.0231	0.0208	<b>0.0188</b>
XGBoost	0.0226	0.0191	0.0213	0.0230
QNN_Q3	0.0132	0.0125	0.0135	0.0120
QNN_Q3_Parallel	0.0125	0.0118	0.0124	<b>0.0107</b>

Table 11. Experimental setup and hyperparameters for the three benchmark tasks, including details for gradient boosting baselines (XGBoost and CatBoost).

Models	Parameter Types	Concrete	Red Wine Quality	High-Dimensional Option Portfolio
<b>Data</b>	Input dimensions	$d = 8$	$d = 11$	$d = \{36, 99, 300\}$
	Samples	1030	1599	1000 simulations $\times$ 10 time steps
	Output dimensions	1	6	$d = \{36, 99, 300\}$
	Data Split	70% Train / 15% Val / 15% Test	70% Train / 15% Val / 15% Test	
<b>XGBoost</b>	Learning Rate	0.1	0.1	0.1
	Tree Depth	$K = \{3, 5, 7, 9\}$	$K = \{3, 5, 7, 9\}$	$K = \{3, 5, 7, 9\}$
	Iterations	5000	5000	1000
<b>CatBoost</b>	Learning Rate	0.1	0.1	0.1
	Tree Depth	$K = \{3, 5, 7, 9\}$	$K = \{3, 5, 7, 9\}$	$K = \{3, 5, 7, 9\}$
	Iterations	5000	5000	1000
<b>DNN</b>	Layers	$L = \{3, 5, 7, 9\}$	$L = \{3, 5, 7, 9\}$	$L = \{3, 5, 7, 9\}$
	Hidden size	64	64	64
	Batch size	full	full	64
	Learning Rate	0.005	0.005	0.01
	Epochs	5000	5000	100
<b>FC VQC</b>	Optimizer	Adam	Adam	Adam
	Layers	$L = \{1, 3, 5, 7, 9\}$	$L = \{1, 3, 5, 7, 9\}$	$L = \{1, 3, 5, 7, 9\}$
	VQC depths	$K = \{3, 5, 7, 9\}$	$K = \{3, 5, 7, 9\}$	$K = \{3, 5, 7, 9\}$
	Batch size	full	full	64
	Learning Rate	0.005	0.005	0.01
	Epochs	5000	5000	100
	Optimizer	Adam	Adam	Adam

Table 12. Detailed architecture specifications for the FC VQC models across the three benchmark tasks.  $Q_n$  denotes an  $n$ -qubit variational block.

Model Type	Concrete (Regression)	Red Wine Quality (Classification)	High-Dimensional Option Portfolio
Type 1	<b>SingleVQC.8</b> ( $L=1$ ) 1 block of $Q_8$	<b>SingleVQC.11</b> ( $L=1$ ) 1 block of $Q_{11}$	–
Type 2	<b>SingleVQC.8</b> ( $L > 1$ ) Input/Hidden layers: 1 block of $Q_8$	<b>SingleVQC.11</b> ( $L > 1$ ) Input/Hidden layers: 1 block of $Q_{11}$	–
Type 3	<b>8t3t1</b> Input/Hidden layers: 3 blocks of $Q_3$ Output layers: 3 blocks of $Q_3 \rightarrow 1$ block of $Q_3$	<b>12t8t6</b> Input/Hidden layers: 4 blocks of $Q_3$ Output layers: 4 blocks of $Q_3$ (Measure 2 qubits/block) $\rightarrow 1$ block of $Q_8$ (Measure 6 qubits)	<b>QNN.Q3 (Sliding Window block mixing)</b> Input/Hidden layers: 12 blocks of $Q_3$ for $d = 36$ 33 blocks of $Q_3$ for $d = 99$ 100 blocks of $Q_3$ for $d = 300$ <b>QNN.Q3.Parallel (Parallel Block)</b> Input/Hidden layers: 12 blocks of $Q_3$ for $d = 36$ 33 blocks of $Q_3$ for $d = 99$ 100 blocks of $Q_3$ for $d = 300$ <b>QNN.Q6 (Fully Connected block mixing)</b> Input/Hidden layers: 6 blocks of $Q_6$ for $d = 36$
Type 4	<b>16t4t1</b> Input/Hidden layers: 4 blocks of $Q_4$ Output layers: 4 blocks of $Q_4 \rightarrow 1$ block of $Q_4$ <b>24t8t3t1</b> Input/Hidden layers: 8 blocks of $Q_3$ Output layers: 8 blocks of $Q_3 \rightarrow 3$ blocks of $Q_3 \rightarrow 1$ block of $Q_3$ <b>32t11t4t1</b> Input/Hidden layers: 11 blocks of $Q_3$ Output layers: 11 blocks of $Q_3 \rightarrow 4$ blocks of $Q_3 \rightarrow 1$ block of $Q_4$ <b>40t14t5t1</b> Input/Hidden layers: 14 blocks of $Q_3$ Output layers: 14 blocks of $Q_3 \rightarrow 5$ blocks of $Q_3 \rightarrow 1$ block of $Q_5$	<b>22t8t6</b> Input/Hidden layers: 8 blocks of $Q_3$ Output layers: 8 blocks of $Q_3$ (Measure 2 qubits/block) $\rightarrow 1$ block of $Q_8$ (Measure 6 qubits) <b>33t12t8t6</b> Input/Hidden layers: 11 blocks of $Q_3$ Output layers: 11 blocks of $Q_3 \rightarrow 4$ blocks of $Q_3 \rightarrow 1$ block of $Q_8$ (Measure 6 qubits) <b>44t15t10t8t6</b> Input/Hidden layers: 15 blocks of $Q_3$ Output layers: 15 blocks of $Q_3 \rightarrow 5$ blocks of $Q_3$ (Measure 2 qubits/block) $\rightarrow 4$ blocks of $Q_3$ (Measure 2 qubits/block) $\rightarrow 1$ block of $Q_8$ (Measure 6 qubits)	–

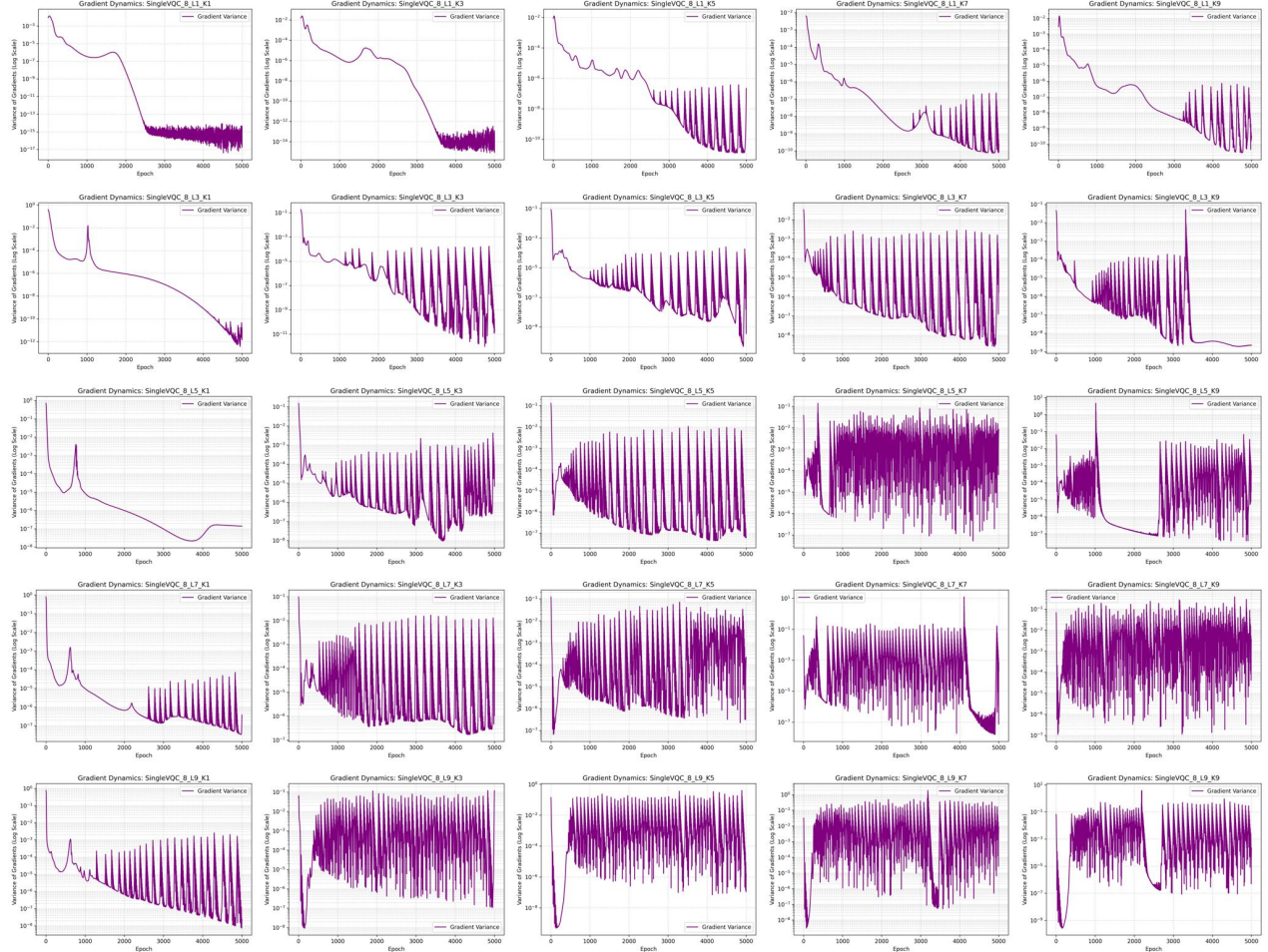
Note: For architectures where the input dimension does not perfectly match the total block capacity (Block Count  $\times$  Qubits), the input vector is zero-padded to fit. For example, in the **8t3t1** model ( $d = 8$ ), one zero value is added to create a 9-dimensional input, fitting exactly into 3 blocks of  $Q_3$ .

Table 13. Trainable parameter counts for Classical DNN versus Multi-layer FC-VQC architectures on the **Concrete Compressive Strength** task ( $d = 8$ ). Columns indicate the parameter count relative to the internal circuit depth  $K$  (or hidden layers  $L$  for the classical DNN). The FC-VQC models require significantly fewer parameters to achieve comparable performance.

Model Type	Layers ( $L$ )	Depth $K = 1$	Depth $K = 3$	Depth $K = 5$	Depth $K = 7$	Depth $K = 9$
<b>Classical Baseline</b>						
DNN ( $d = 8$ )	–	4,801	13,121	21,441	29,761	38,081
<b>Quantum Architectures</b>						
8t3t1	1	90	270	450	630	810
	3	144	432	720	1,008	1,296
	5	198	594	990	1,386	1,782
	7	252	756	1,260	1,764	2,268
	9	306	918	1,530	2,142	2,754
16t4t1	1	156	468	780	1,092	1,404
	3	252	756	1,260	1,764	2,268
	5	348	1,044	1,740	2,436	3,132
	7	444	1,332	2,220	3,108	3,996
	9	540	1,620	2,700	3,780	4,860
24t8t3t1	1	252	756	1,260	1,764	2,268
	3	396	1,188	1,980	2,772	3,564
	5	540	1,620	2,700	3,780	4,860
	7	684	2,052	3,420	4,788	6,156
	9	828	2,484	4,140	5,796	7,452
32t11t4t1	1	345	1,035	1,725	2,415	3,105
	3	543	1,629	2,715	3,801	4,887
	5	741	2,223	3,705	5,187	6,669
	7	939	2,817	4,695	6,573	8,451
	9	1,137	3,411	5,685	7,959	10,233
40t14t5t1	1	438	1,314	2,190	3,066	3,942
	3	690	2,070	3,450	4,830	6,210
	5	942	2,826	4,710	6,594	8,478
	7	1,194	3,582	5,970	8,358	10,746
	9	1,446	4,338	7,230	10,122	13,014

## E. Gradient Dynamics Analysis: Concrete Compressive Strength

This section presents the full training dynamics for the Concrete Compressive Strength regression task ( $d = 8$ ). The following plots visualize the variance of gradients across epochs for different architectural configurations, illustrating the transition from barren plateaus (in monolithic models) to healthy, stable gradients (in modular FC-VQCs).



**Figure 4.** Gradient Dynamics on Concrete (SingleVQC\_8). The grid displays gradient variance over training epochs. **Rows** correspond to Stacking Layers  $L \in \{1, 3, 5, 7, 9\}$  and **Columns** to Internal Depth  $K \in \{1, 3, 5, 7, 9\}$ . Row 1 ( $L = 1$ ) represents the monolithic **Type 1** baseline, which immediately succumbs to barren plateaus (vanishing variance). Rows 2–5 (**Type 2**) show that simply stacking monolithic blocks fails to stabilize the gradients.

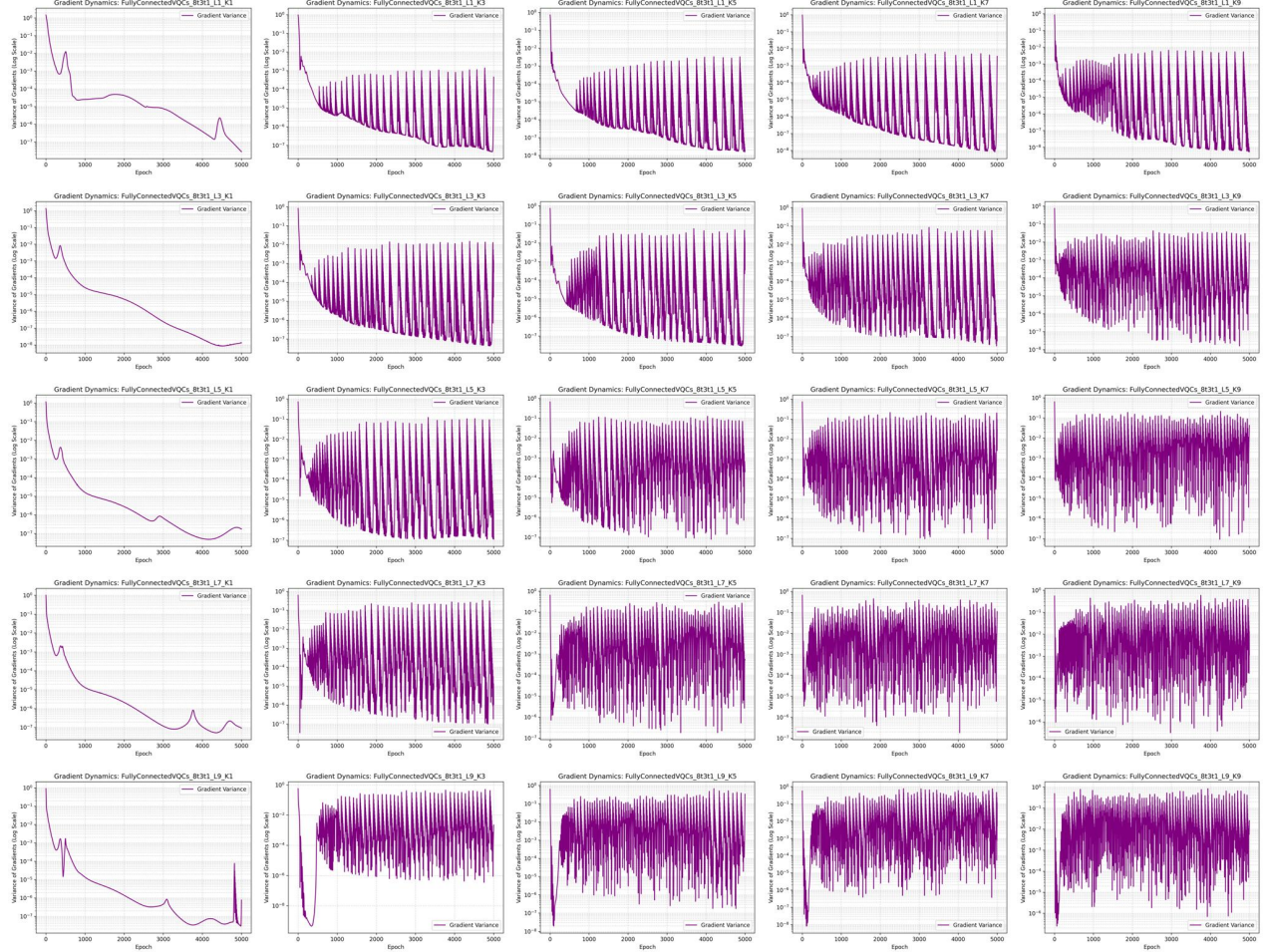


**Figure 5. Gradient Dynamics on Concrete (Type 3: 8t3t1).** Grid layout: Rows  $L \in \{1..9\}$ , Columns  $K \in \{1..9\}$ . Unlike the SingleVQC baseline, this modular fully-connected architecture begins to show signs of trainability. While extremely shallow blocks ( $K = 1$ , Column 1) still face barren plateaus, deeper configurations ( $K \geq 3$ ) combined with stacking ( $L \geq 3$ ) exhibit non-zero, healthy gradient variance.

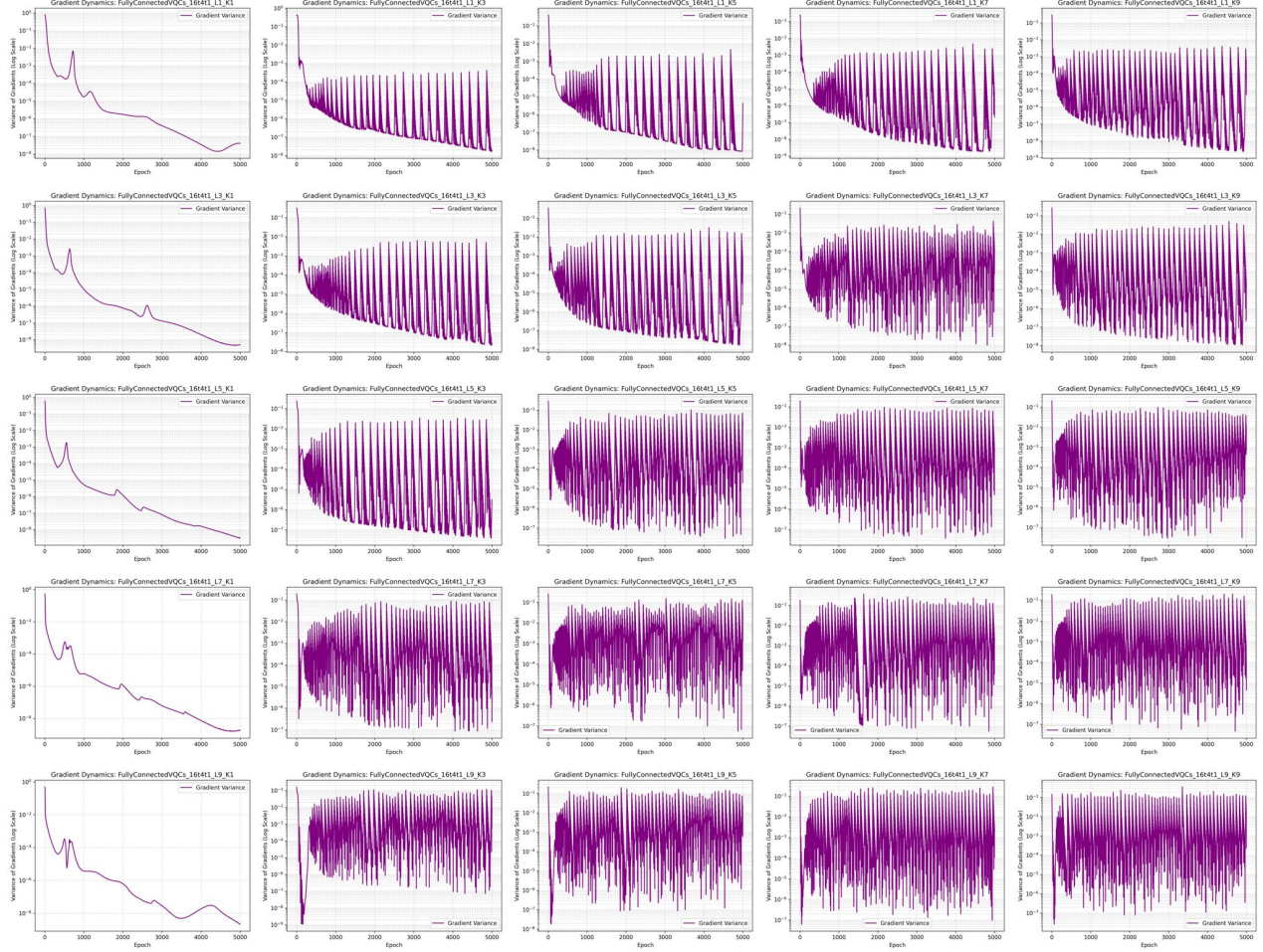
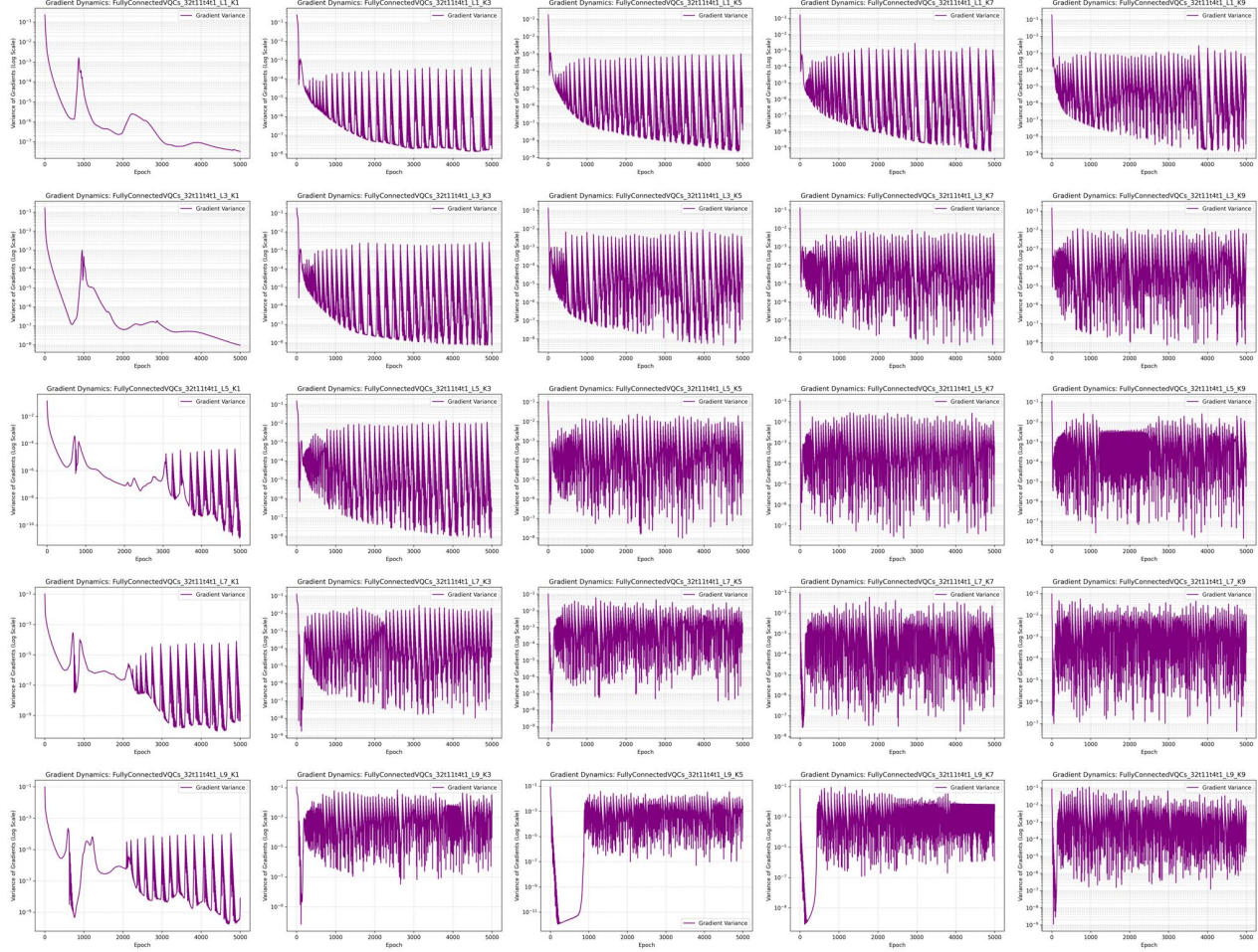
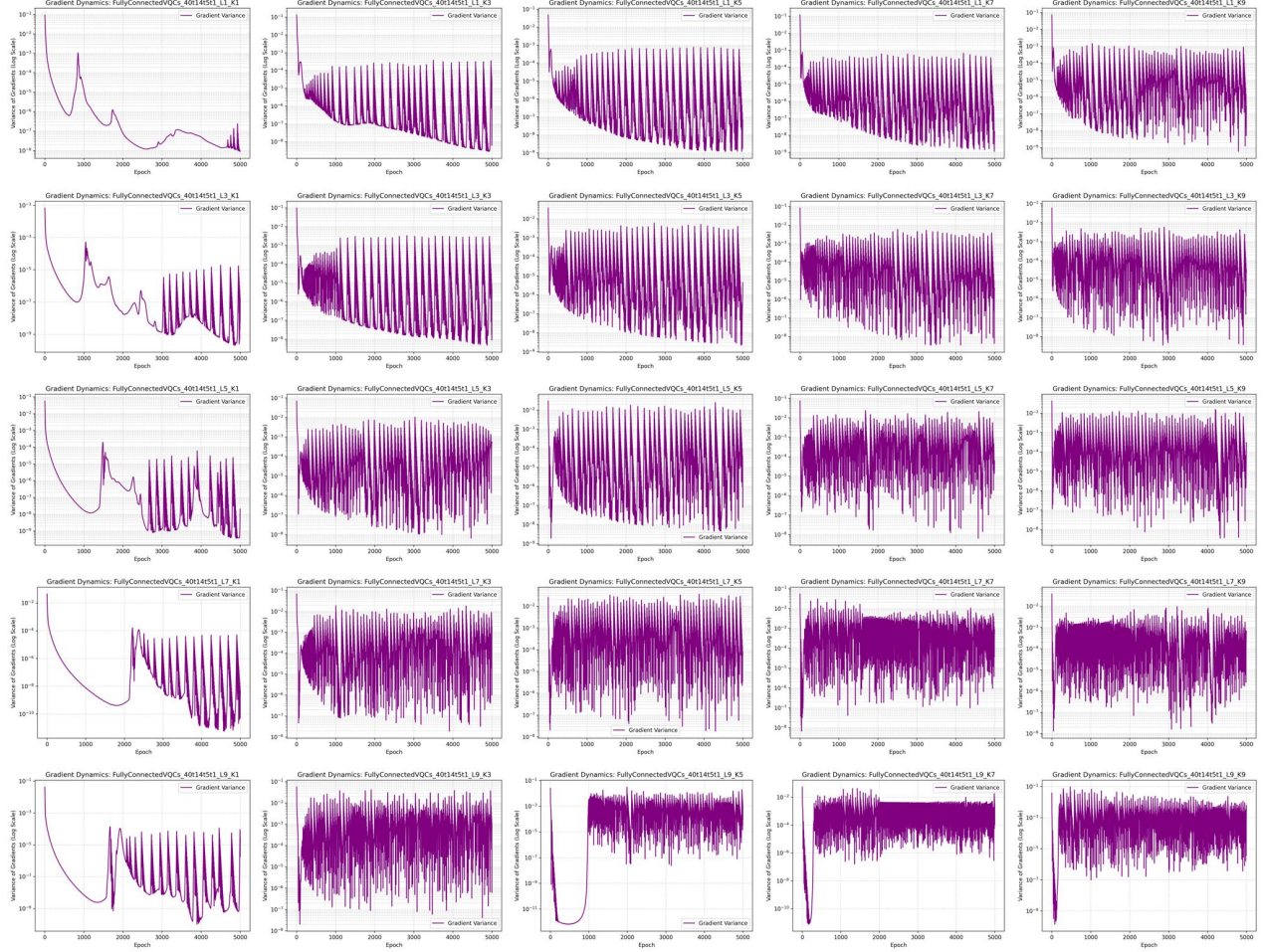


Figure 6. Gradient Dynamics on Concrete (Type 4: 16t4t1). Grid layout: Rows  $L \in \{1..9\}$ , Columns  $K \in \{1..9\}$ . With feature expansion and slightly larger blocks ( $q = 4$ ), the “healthy” regime expands. Note that the variance in the lower-right quadrant (High  $L$ , High  $K$ ) stabilizes significantly compared to Type 1/2, avoiding exponential decay.



**Figure 7. Gradient Dynamics on Concrete (Type 4: 32t11t4t1).** Grid layout: Rows  $L \in \{1..9\}$ , Columns  $K \in \{1..9\}$ . This architecture, which achieves parity with classical gradient boosting, displays robust training dynamics. The plots for  $K \geq 3$  show sustained gradient variance throughout the training process, confirming that the high test accuracy is supported by a trainable optimization landscape.



**Figure 8. Gradient Dynamics on Concrete (Type 4: 40t14t5t1).** Grid layout: Rows  $L \in \{1..9\}$ , Columns  $K \in \{1..9\}$ . Even with the highest parameter count and depth, the modular structure prevents barren plateaus. The gradients in the deep regimes ( $L \geq 5, K \geq 5$ ) remain healthy and oscillatory, validating the scalability of the FC-VQCs.